remote sensing

Article

Satellite Advanced Spaceborne Thermal Emission and Reflection Radiometer Mineral Maps of Australia Unmixed of Their Green and Dry Vegetation Components: Implications for Mapping (Paleo) Sediment Erosion–Transport–Deposition Processes

Tom Cudahy * and **Liam Cudahy †**

C3DMM Pty Ltd., P.O. Box 335, Balingup, WA 6253, Australia
* Correspondence: thomas.cudahy@c3dmm.com
† deceased.

Abstract: The 2012 satellite ASTER geoscience maps of Australia were designed to provide public, web-accessible, and spatially comprehensive surface mineralogy for improved mapping and solutions to geoscience challenges. However, a number of the 2012 products were clearly compromised by variable green and/or dry vegetation cover. Here, we show a strategy to first estimate and then unmix the contributions of both these vegetation components to leave, as residual, the target surface mineralogy. The success of this unmixing process is validated by (i) visual suppression/removal of the regional climate and/or local fire-scar vegetation patterns; and (ii) pixel values more closely matching field sample data. In this process, we also found that the 2012 spectral indices used to gauge the AlOH content, AlOH composition, and water content can be improved. The updated (new indices and vegetation unmixed) maps reveal new geoscience information, including: (i) regional "wet" and "dry" zones that appear to express "deep" geological characters often expressed through thick regolith cover, with one zone over the Yilgarn Craton spatially anti-correlated with Archaean gold deposits; (ii) a ~1000 km wide circular feature over the Lake Eyre region defined by a rim of abundant "muscovite" that appears to coincide with opal deposits; (iii) a N–S zonation across the western half of the continent defined by abundant muscovite in the south and kaolinite in the north, which appears to reflect opposing E ↔ W aeolian sediment transport directions across the high-pressure belt; (iv) various paleo-drainage networks, including those over aeolian sand covered the "lowlands" of the Canning Basin, which are characterized by low AlOH content, as well as those over eroding "uplands", such as the Yilgarn Craton, which have complicated compositional patterns; and (v) a chronological history of Miocene barrier shorelines, back-beach lagoons, and alluvial fans across the Eucla Basin, which, to date, had proved elusive to map using other techniques, with potential implications for heavy mineral sand exploration. Here, we explore the latter three issues.

Keywords: satellite; ASTER; Australian continent; dry vegetation unmixing; AlOH minerals; quartz sand; soil moisture; paleo-geomorphology

check for updates

Citation: Cudahy, T.; Cudahy, L. Satellite Advanced Spaceborne Thermal Emission and Reflection Radiometer Mineral Maps of Australia Unmixed of Their Green and Dry Vegetation Components: Implications for Mapping (Paleo) Sediment Erosion–Transport–Deposition Processes. *Remote Sens.* **2024**, *16*, 1740. https://doi.org/10.3390/rs16101740

Academic Editors: Ana Cláudia Teodoro, Joana Cardoso-Fernandes and Alexandre Lima

Received: 5 April 2024
Revised: 4 May 2024
Accepted: 9 May 2024
Published: 14 May 2024

1. Introduction

The launch of the ASTER (Advanced Spaceborne Thermal Emission and Reflection Radiometer) satellite imaging sensor [1] in 1999 and its subsequent successful program of global mapping the Earth's entire land surface (~six repeats) <70° latitude using its "mineral-tuned", multi-spectral VNIR-SWIR-TIR (visible to near infrared; shortwave infrared; thermal infrared) sensors presents an opportunity to map a diverse suite of process-critical minerals (e.g., rock type, metamorphic alteration, weathering, and transported cover). This "mineral mapping" is based on the spectroscopic measurement of electromagnetic energy and its interaction with minerals [2], which have diagnostic, wavelength-dependent absorption and/or reststrahlen features. For example, absorption at 2200 nm is caused by the (polarized) vibration of di-octahedrally-coordinated Al-OH bonds in phyllosilicates like muscovite [3] and kaolinite [4]. This 2200 nm absorption is specifically targeted by ASTER band 6.

The first continental-scale ASTER mineral maps were publicly released in 2012 for Australia [5]. These geoscience maps are based on spectral band ratios, which target a range of mineral-diagnostic features across ASTER's three wavelength modules. These modules include: (i) three bands in VNIR (15 m pixel resolution); (ii) six bands in the SWIR (30 m pixel resolution); and (iii) five bands in the TIR (90 m pixel resolution). The 2012 ASTER maps of Australia have since been investigated for a range of geoscience applications [6–15], though their value has arguably been limited by both the use of a heavy green vegetation mask [5], which culled >40% of all pixels (100% in more wet, vegetated regions), with a number of products especially over arid regions showing the effects of variable dry vegetation cover [6]. Therefore, a new strategy for correcting vegetation is required to improve the geoscience value of ASTER imagery [7].

Estimating the green vegetation content is relatively simple using ASTER as its VNIR bands target specific plant properties, like chlorophyll absorption (ASTER bands 1 and 2) and the NIR photosynthetically-active reflectance plateau (ASTER band 3) [16]. However, ASTER was not designed to measure dry vegetation features, like cellulose absorption at 2080 nm or lignin absorption at 2270 nm [17]. This deficiency in sensor design is common to all satellite multi-spectral systems launched since ERTS-1 in 1972 [16]. This despite dry vegetation being the dominant vegetation cover type across much of the Earth's drier regions as well as during seasonal senescence in more temperate latitudes. Thus, accurate estimations of the dry vegetation component from multispectral data are (and will remain) problematic [7,18–22].

Here, we test dry vegetation indices that use different wavelength modules of ASTER, namely: (i) an NIR-SWIR index [22], which targets the shoulder of the 2080 nm cellulose and 2270 nm lignin features, though these also overlap with mineral absorptions (e.g., chlorite); and (ii) a TIR index [22], which targets a broad cellulose feature centered at 10,500 nm [17,23], though this also overlaps with mineral reststrahlen features (e.g., quartz). That is, both indices are likely to yield residual mineral-related artifacts in certain geological environments. These ASTER dry vegetation indices, as well as a green vegetation index, are then used in an unmixing strategy [7,21,24–33] to unmix the Australian ASTER reflectance/emissivity mosaic [34], which comprises >3000 cross-calibrated ASTER images that were collected between 2000 and 2007 [35]. We also reassess a number of indices from the 2012 Australian ASTER geoscience product suite [5] to determine whether they are optimized for mapping mineral-sensitive (paleo) erosion–transport–deposition processes. We validate these results by (i) observing how well vegetation effects evident as fire scars and regional rainfall patterns are suppressed/removed at different scales; and (ii) comparing these ASTER indices with laboratory spectral and physiochemical measurements of surface samples collected as part of the National Geochemical Survey of Australia (NGSA) [36–38].

Along this journey, new geoscience information is revealed using these updated ASTER mineral maps about the geology and mineralized systems across Australia, including: (i) Archaean hydrothermal gold across the Yilgarn Craton; (ii) opal (silica) development across central Australia; and (iii) natural, REDOX-related hydrogen degassing [39]. These are to be tackled, ideally, in future work. But here we focus on the networks of (paleo) rivers and marine basins that were active during the Cenozoic, when sea levels and rainfall were higher [40–50]. Some of these paleo-systems are now the focus of heavy mineral sand and valley–calcrete–uranium exploration [43,44,48].

To date, paleo-valleys have been primarily mapped using digital elevation models (DEMs) [51] and satellite thermal infrared imagery (e.g., NOAA-AVRR and ASTER) [41,50], with the latter sensing surface kinetic temperature patterns best observed during stable (no wind) night-time conditions [41,50]. Other "deeper" geophysical sensing techniques have also been tested, such as airborne electromagnetics, targeting saline groundwater [52]. However, surface sensing techniques, like airborne gamma radiometrics [53] and the 2012

ASTER products [5], have been less attractive because of the perception that the surface-detected composition is too complex to unravel [54]. We instead argue that accurate surface mineral maps that are diagnostic of erosion–transport–deposition processes will not only assist geoscientists in unravelling the surface regolith complexity but also reveal new and valuable geoscience information/knowledge not obtainable from any other mapping data type.

Here, we focus on improving the accuracy/value of a selection of the 2012 ASTER mineral products [5] using this vegetation unmixing strategy. These "regolith" products include: (i) the "silica index" [55,56], which is largely driven by the content of quartz sand; (ii) "AlOH content", which is a gauge of the amount of "weathering-related", AlOH-bearing "clay" minerals [57]; (ii) "AlOH composition", which is sensitive to the species of "clay" minerals, including illite (~muscovite), montmorillonite, and kaolinite; and (iii) water content or "soil moisture" [6], which can also be driven by the type of clay mineral, like montmorillonite = "wet" while kaolinite = "dry" [6]. Not included here but also likely to assist in "unravelling" the complexity of the regolith are other ASTER products [5] such as REDOX-related ferric oxyhydroxides and ferrous oxides/silicates/carbonates, especially given their potential importance for hydrogen exploration [39].

Based on the updated ASTER mineral maps, we therefore asked the following: (i) are (paleo-) rivers, shorelines, and fans/deltas better expressed and/or is new geoscience information revealed; (ii) does this compositional information provide clues regarding understanding Cenozoic sediment transport systems, especially sediment provenance, depositional chronology, the paleo-climate, flow direction, energy of depositional environments, and tectonics/the climate; and (iii) does this information create new opportunities for mineral exploration?

In summary, the primary objective of this paper is (i) to describe a vegetation unmixing method that compensates for both the green components and, especially, the dry vegetation components using the ASTER's limited spectral band configuration to generate more accurate maps of surface mineral information (compared with [5]); and (ii) to demonstrate the efficacy of the updated mineral maps for mapping paleo-geomorphic systems, especially those across more arid regions of Australia obscured by dry vegetation cover.

2. Materials and Methods

2.1. ASTER Data Pre-Processing

The 2012 Australian cross-calibrated ASTER reflectance (VNIR and SWIR bands at 30 m pixel resolution) and emissivity (TIR bands at 90 m pixel resolution) mosaics [34] were processed using the software package, Environment for Visualizing Images (ENVI) (Version 3.5), to generate a single mosaic combining all 14 VNIR, SWIR, and TIR bands resampled to a 100 m pixel size (nearest neighbor sampling) to allow for vegetation unmixing across all three ASTER wavelength modules. Essential to the task of isolating and enhancing compositional information is the process of pixel normalization, such as band ratios [58], which cancels the often-dominant, multiplicative, wavelength-independent effects, such as topographic illumination, surface scattering, and albedo [59,60]. This step is only effective when all of the additive effects, like atmospheric scattering (in the VNIR) and instrument error (e.g., the ASTER SWIR cross-talk effect) [61], have first been corrected. Given this, then, the resultant normalized images should appear "flat" over variable topographic illumination, with areas in deep shade (and water in the SWIR) appearing as "salt-and-pepper" (shot) noise. The additive error assessment and correction step was implemented as part of the 2012 Australian ASTER reflectance mosaic generation [5].

2.2. Vegetation Cover Issue

The vegetation cover challenge [62] is demonstrated in Figure 1, where the published paleo-geomorphic features [47], like rivers (cyan lines), shorelines and lagoons (yellow lines), are obscured by a patchwork of variable vegetation cover. The 2012 ASTER "AlOH" content (Figure 1b) and "silica index" (Figure 1c) products [5] are especially obscured by the dry vegetation component, which is highlighted by the edges of the fire scars (red lines), while the 2012 ASTER "iron oxide content" product (Figure 1d) is instead affected by green vegetation (green lines). That is, the green and dry vegetation cover not only compromises the mapping of paleo-geomorphic elements (Figure 1b–d) but also disrupts the integrity of the pixel spectral mineral signatures.

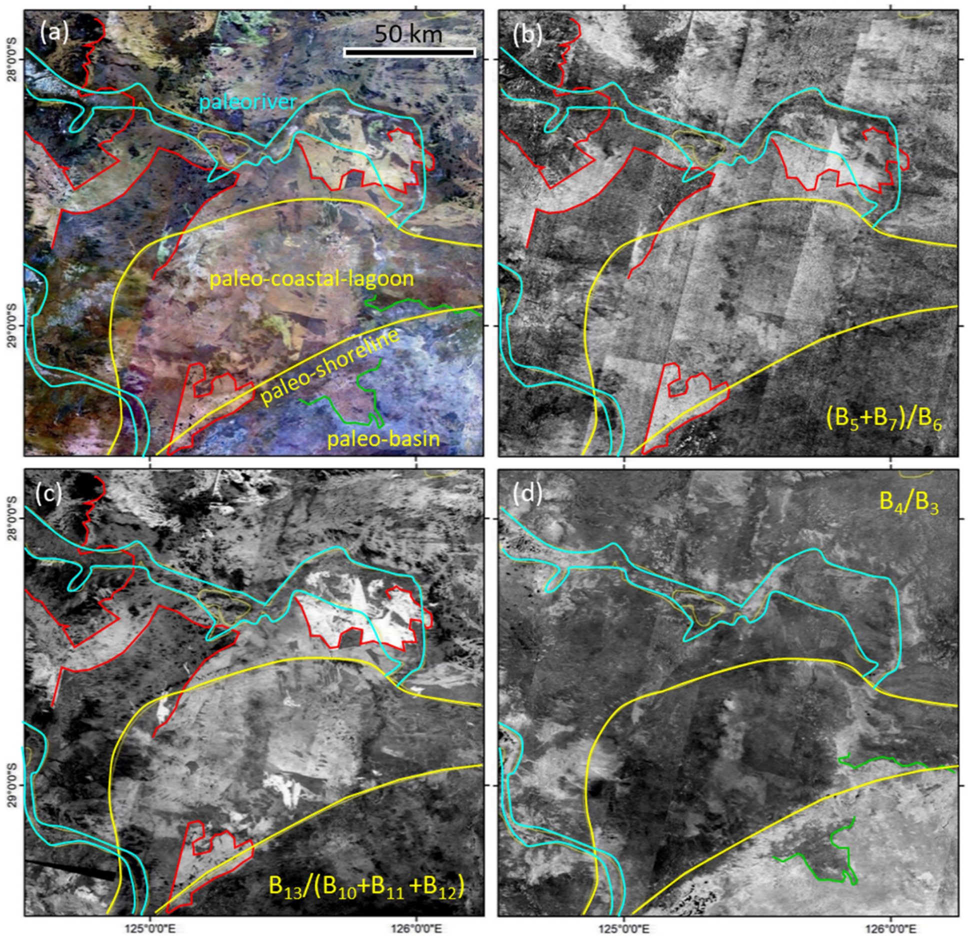

Figure 1. Satellite ASTER mosaics of an area in Western Australia showing elements of an Eocene paleo-geomorphic system (yellow and cyan polylines) [47]. Examples of fire scars causing abrupt changes in green vegetation (green lines) and dry vegetation (red lines) are highlighted. (**a**) False color composite (R:G:B—ASTER bands 3:2:1) with red tones showing photosynthetically-active green vegetation. (**b**) The 2012 ASTER "clay mineral" content ((B_5 + B_7)/B_6) [5]. (**c**) The 2012 ASTER "silica index" (B_{13}/(B_{10} + B_{11} + B_{12}) [5]. (**d**) The 2012 ASTER "iron oxide" content (B_4/B_3) [5].

2.3. ASTER Vegetation Unmixing Process

Three ASTER vegetation indices were tested using ENVI (Version 3.5), including:

(i) A green vegetation index:

$$V^{green} = (B_3 - B_2)/(B_2 + B_3) \tag{1}$$

This index is based on the normalized difference vegetation index [16], which targets photosynthetic activity and cancels cross-track surface scattering variation.

(ii) A SWIR-derived dry-vegetation index [21]:

$$V^{dry}_{SWIR} = [(0.3 \times B_4) + B_6)/(0.5 \times B_3 + (B_5 + B_7)] \tag{2}$$

This dry vegetation index targets the cellulose and lignin absorption rates (ASTER bands 5 and 7, respectively), as well as a lack of the photosynthesis-active NIR plateau [17] (ASTER bands 3 and 4). It is also more comprehensive than the ASTER dry vegetation index of [18], which used a ratio of ASTER bands 6 and 7 and, thus, did not consider the impact of "clay" mineral-related AlOH absorption.

(iii) A TIR-derived dry-vegetation index [22]:

$$V_{TIR}^{dry} = B_{10} / \left(B_{11} + B_{13} + B_{14}\right) \quad (3)$$

This TIR-based index (Equation (3) targets a broad reflectance peak (emissivity low) for dry vegetation at wavelengths > 9200 nm (centered at 10,500 nm) (ASTER bands 13 and 14) [17,22,23,63]. ASTER band 12, centered at 9100 nm, was omitted because it is where clay minerals typically have their reflectance peak (i.e., minimize an inverse clay silicate mineral response). Band 10 is centered at 8250 nm, positioned over a quartz reflectance peak, while band 11 (8625 nm) in the denominator helps to minimize the contribution of quartz.

The vegetation unmixing process begins by assessing for suitable mixing behaviors. This can be achieved using a 2-dimensional (2D) scattergram, with the vegetation index (Equations (1)–(3)) plotted against the target mineral index. An "ideal" mixing pattern is where the data cloud approximates a right triangle, with its perpendicular corner positioned at zero–zero. Given this geometry for both green vegetation (V^{green}) and dry vegetation (V^{dry}) with the target mineral index (T), the process of unmixing for a given pixel "i" can be subsequently described as follows:

$$T_i^{unmixed} = T_i^{mixed} + a \times V_i^{green} + b \times V_i^{dry} \quad (4)$$

The gains "a" and "b" were iteratively determined using the image data by gauging how well they suppress vegetation-related "edge" effects, such as fire scars (Figure 1), with the assumption being that the surface mineral signature across these "edges" is more slowly changing. A suitable gain (i) suppresses these edge effects across a wide range of (all) geological surface compositions for all areas, and (ii) generates a dimensionless 2D data cloud. Note that we first scaled all input spectral indices between 0 and 1 for simplicity. Though not included in Equation (4), there is also wavelength-dependency involved in the process. For example, green vegetation can affect minerals with diagnostic VNIR spectral features, such as iron oxides (Figure 1d), whereas dry vegetation can affect SWIR- and TIR-active minerals, like the 2200 nm AlOH absorbers (Figure 1b) and silicates (Figure 1c), respectively; that is, those wavelengths where vegetation is "aspectral" (transparent and with no spectral features) require no correction.

2.4. NGSA Validation Data

The NGSA samples used for the validation of the ASTER products comprise >1000 unconsolidated, fluvial-channel (including paleo-channels) overbank samples taken from the top 10 cm of the regolith of (paleo) river catchments across Australia [36]. A range of laboratory measurements were taken from these samples, including geochemistry, particle size distribution, and VNIR–SWIR–TIR reflectance measurements. The reflectance data were collected using an Analytical Spectral Device (ASD) FieldspecPro-3 bi-directional reflectance spectrometer and a Bruker Vertex 70 directional–hemispherical spectrometer [38]. These spectral data were then convolved to ASTER bandpass responses using ENVI image processing software (Version 5.3).

Three high spectral resolution, NGSA absorption band-depth indices [58] were used for the assessment/validation of ASTER indices/products, namely:

(i) AlOH clay absorption depth centered at 2207 nm:

$$(b_{2140} + b_{2260}) / b_{2207} \quad (5)$$

(ii) Kaolinite absorption depth centered at 2165 nm:

$$(b_{2140} + b_{2207})/b_{2165} \tag{6}$$

(iii) Water absorption depth centered at 1915 nm [64]:

$$(b_{1850} + b_{2100})/(b_{1910} + b_{1920}) \tag{7}$$

Note here the use of the lower-case "b" mnemonic for the ASD indices in contrast to the upper-case "B" used for the ASTER indices (Equations (1)–(3)). Statistical assessment (Table 1) for the same 165 NGSA samples used for the 2016 study [6]. Correlations here are deemed significant at the 90% confidence level if the regression coefficient of correlation (R^2) exceeds 0.35. All relationships were tested using linear functions, though some R^2 values would have been improved if non-linear functions were fitted instead.

Table 1. Statistical results for 165 random NGSA samples [6]. Significant (linear) correlations (R^2 = 0.35 at the 90% confidence level) are highlighted in bold. Inverse relationships are underlined.

	%Clay	**Al/(Al + Si)**	**CIA**	**LOI**	**(b_{2140} + b_{2207})/b_{2165}**	**(b_{2140} + b_{2260})/b_{2208}**	**(b_{1850} + b_{2100})/(b_{1910} + b_{1920})**
% clay	1.00						
Al/(Al + Si)	**0.45**	1.00					
CIA	0.00	0.00	1.00				
LOI	0.31	**0.48**	0.05	1.00	$\underline{0.12}$		
(b_{2140} + b_{2260}/b_{2207}	0.07	0.03	0.27	0.03	0.02	1.00	
(b_{1850} + b_{2100})/(b_{1910} + b_{1920})	**0.44**	0.20	0.01	0.10	**$\underline{0.37}$**	0.30	1.00
(b_{2140} + b_{2207}/b_{2165}	$\underline{0.30}$	$\underline{0.16}$	0.08	$\underline{0.12}$	1.00	0.02	**$\underline{0.37}$**
(B_5 + B_7)/B_6	0.10	0.03	0.23	0.04	0.00	$\underline{0.23}$	0.33
(B_7)/(B_5 + B_6)	$\underline{0.13}$	$\underline{0.16}$	0.22	**$\underline{0.35}$**	**0.51**	$\underline{0.08}$	0.14
B_7/B_6	0.00	$\underline{0.03}$	0.30	$\underline{0.22}$	0.20	**0.69**	0.00
(B_6 + B_7)/(B_8 + B_9)	**0.45**	0.34	0.01	0.21	0.23	0.29	**0.84**
(B_6 + B_7)/B_8	0.33	**0.39**	0.00	0.33	$\underline{0.20}$	0.11	**0.60**
B_8/B_9	**0.47**	0.20	0.08	0.06	$\underline{0.19}$	$\underline{0.09}$	**0.88**
B_8	$\underline{0.30}$	$\underline{0.25}$	$\underline{0.10}$	$\underline{0.13}$	0.08	$\underline{0.08}$	$\underline{0.32}$
B_9	$\underline{0.35}$	$\underline{0.27}$	$\underline{0.11}$	$\underline{0.13}$	0.10	$\underline{0.12}$	**$\underline{0.39}$**
(B_5 + B_6 + B_7 + B_8 + B_9)/B_9	**0.48**	0.28	0.03	0.14	$\underline{0.26}$	**0.36**	**0.92**
(B_5 + B_6 + B_7 + B_8)/B_8	**0.38**	**0.39**	0.01	0.31	$\underline{0.31}$	0.11	**0.71**
(B_5 + B_6 + B_8)/(B_7 + B_9)	**0.53**	0.31	0.00	0.22	**$\underline{0.51}$**	0.13	**0.81**
(B_5 + B_8)/(B_7 + B_9)	**0.52**	0.31	0.00	0.22	**$\underline{0.50}$**	$\underline{0.02}$	**0.90**
B_7/B_8	0.25	0.23	0.06	0.07	$\underline{0.03}$	**0.62**	**0.57**
B_7/B_5	$\underline{0.32}$	$\underline{0.28}$	0.30	$\underline{0.34}$	**0.66**	0.02	**$\underline{0.49}$**

Given that at ASTER spectral resolution only two 2165–2200 nm absorbing mineral components are measurable (degrees of freedom), we described these endmembers as being either "muscovite" or "kaolinite". The "muscovite" endmember can also include minerals like paragonite, phengite, lepidolite, brammallite, illite, and montmorillonite, while the "kaolinite" endmember can also include minerals like dickite, nacrite, halloysite, pyrophyllite, and alunite.

3. Results

3.1. NGSA—ASTER Mineral Indices

Table 1 presents the R^2 results of the spectral (ASD and ASD-ASTER convolved), chemical, and particle-size parameters for the 165 randomly selected NGSA samples. The seven "target" parameters include:

1. The percentage of clay-sized particles (<2-micron size) "%clay".
2. The geochemical indices:
   - Al/(Al + Si), which is an indicator of the proportion of Al-bearing clay minerals to coarser quartz grains;
   - Al/(Al + Ca + Mg + Na + K), i.e., based on the chemical index of alteration called the CIA [65];
   - Loss-on-ignition (LOI), which is a measure of the volatiles released after heating, including water, organic compounds, and carbonates [66].
3. ASD continuum-removed absorption depths, namely:
   - AlOH absorption at 2207 nm (Equation (5));
   - Kaolin absorption at 2165 nm (Equation (6));
   - Water absorption at 1915 nm (Equation (7)).

3.2. NGSA—%Clay

There is no correlation between the NGSA %clay particle size and the 2200 nm absorption depth indices: (i) $(b_{2140} + b_{2260})/b_{2207}$ (R^2 = 0.07); (ii) $(B_5 + B_7)/B_6$ (R^2 = 0.10); and (iii) B_7/B_6 (R^2 = 0.00) (Table 1), though there is correlation with the Al/(Al + Si) (R^2 = 0.45) and water-related indices: (i) 1900 nm absorption depth (R^2 = 0.44); (ii) $(B_6 + B_7)/(B_8 + B_9)$ (R^2 = 0.45); (iii) (B_8/B_9) (R^2 = 0.47); (iv) $(B_5 + B_6 + B_7 + B_8 + B_9)/B_9$ (R^2 = 0.48); and (v) $(B_5 + B_8)/(B_7 + B_9)$ (R^2 = 0.52). This can be explained by (i) the effect of increased hydrogen bonding of water molecules on finer particle grains; (ii) the role of clay-sized, non-AlOH-bearing minerals like feldspars, which do not have a 2200 nm absorption; and/or (iii) the effect of decreasing particle size on the optical depth, which results in shallower absorption features [67].

3.3. NGSA—Water Content

Unlike the ASTER's VNIR bands, all of the ASTER's SWIR bands show inverse relationships (better modelled using an exponential decay function) with the ASD 1900 nm water absorption depth (Equation (7)), with correlations increasing with the ASTER's SWIR band number. That is, ASTER band 9 has the highest correlation (R^2 = 0.39), followed by ASTER band 8 (R^2 = 32). This is consistent with the "shoulder" effect to the major, fundamental stretching vibration of molecular water at ~2700 nm [64,68–70]. Thus, ratios with ASTER band 9 in the denominator generate higher correlations; for example: (i) B_8/B_9 (R^2 = 0.88); (ii) $(B_6 + B_7)/(B_8 + B_9)$ (R^2 = 0.84) [6]; (iii) $(B_5 + B_8)/(B_7 + B_9)$ (R^2 = 0.90); and (iv) $(B_5 + B_6 + B_7 + B_8 + B_9)/B_9$ (R^2 = 0.92). The latter two also yield significant correlations with the 2165 and 2207 nm absorption depths (Equations (5) and (6)), respectively). Replacing ASTER band 9 with band 8, to simulate the WV-3 satellite sensor data, also yields a significant correlation with the 1900 nm water absorption depth (Table 1).

3.4. NGSA—AlOH Clay Content

The 2012 ASTER's AlOH content ratio $(B_5 + B_7)/B_6$ is not correlated (weakly anti-correlated) with the ASD 2200 nm absorption depth (Equation (5)) (Table 1). ASTER indices that do show significant correlations include (i) B_7/B_6 (R^2 = 0.69) and (ii) B_7/B_8 (R^2 = 0.62). There is no correlation with respect to the B_7/B_5 ratio (R^2 = 0.02), which means that ASTER band 5 should not be used for gauging the 2200 nm AlOH absorption depth. Using ASTER band 8 for this purpose is also problematic, as a range of minerals (for example, chlorite, jarosite, and gibbsite), which are not well represented in the NGSA sample suite, also absorb in the ~2250 nm wavelength region. Thus, we recommend using the ASTER B_7/B_6 ratio for gauging the 2200 nm AlOH absorption depth.

3.5. NGSA—AlOH Clay Composition

No ASTER or ASD spectral measure was found to correlate with the CIA geochemical index ($Al_2O_3/(Al_2O_3 + CaO^* + Na_2O + K_2O) \times 100$), including the ASD 2165 nm absorption depth (Equation (6)) ($R^2 = 0.08$; Table 1). Given that the 2165 nm absorption in these NGSA samples is caused by kaolin, we thereby conclude that the CIA geochemical index is not a reliable gauge of kaolin content. Furthermore, common regolith minerals, like calcite ($CaCO_3$) and muscovite ($KAl_2(AlSi_3O_{10})(F,OH)_2$) [71], would adversely affect any clay mineral interpretation using the CIA.

The ASD 2165 nm kaolinite absorption index (Equation (6)) shows significant correlations with (i) B_7/B_5 ($R^2 = 0.66$); (ii) $B_7/(B_5 + B_6)$ ($R^2 = 0.51$); (iii) $(B_5 + B_8)/(B_7 + B_9)$ ($R^2 = \underline{0.50}$); and (iv) $B_5 + B_8)/B_7$ ($R^2 = \underline{0.47}$). All of these indices have opposing use of ASTER bands 5 and 7, such that we recommend using ASTER B_7/B_5 for gauging the 2165 nm kaolin absorption depth, but with a caveat; that is, the effects of spectral resolution must also be addressed. This is because B_7/B_5 is significantly correlated with B_7/B_6 ($R^2 = 0.38$) (Figure 2b), while there is no correlation ($R^2 = 0.00$) between the ASD 2200 and 2165 nm absorptions depths (Equations (5) and (6)) (Figure 2a). This dissimilarity is demonstrated in Figure 2, where at a 10 nm spectral resolution (Figure 2a), the 2D data cloud resembles an equilateral triangle (gray-dashed polygon) with three apical endmembers/edgemembers, namely: (i) no AlOH clay; (ii) abundant kaolinite; and (iii) abundant muscovite, while at ASTER's 40 nm spectral resolution (Figure 2b), the 2D data cloud approximates an inclined isosceles triangle (gray-dashed polygon), with its major axis correlation representing AlOH content and its smaller orthogonal axis representing "AlOH-composition" (kaolinite $\leftrightarrow$ muscovite). Note that the slope of the major axis in the NGSA data (Figure 2b) is similar to that of the Australian ASTER data (Figure 2c).

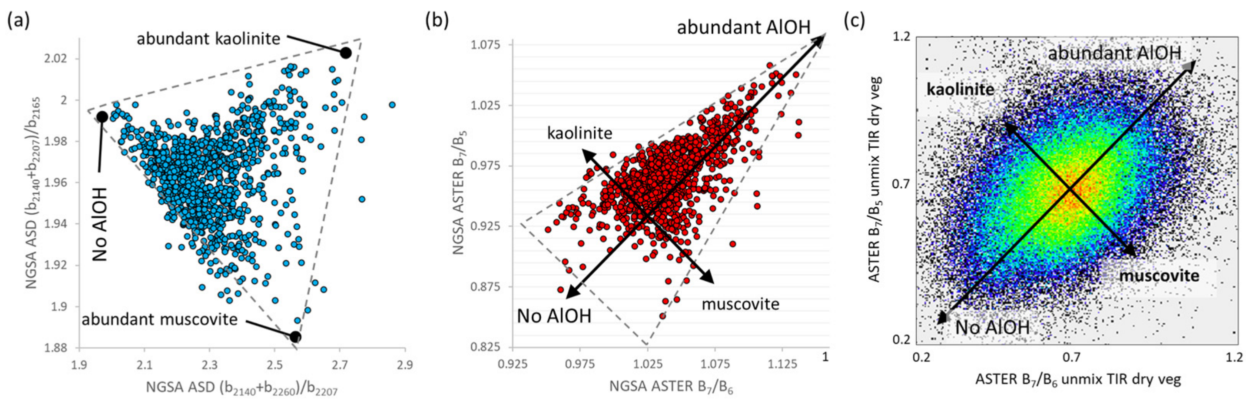

Figure 2. Scattergrams of spectral parameters targeting the relative depths of the 2165 and 2207 nm absorption rates, both of which are sensitive to AlOH clay minerals. (**a**) All NGSA ASD data at a 10 nm spectral resolution. (**b**) All NGSA ASD data at a 40 nm ASTER/WV3 spectral resolution. (**c**) ASTER dry vegetation unmixed clay composition ratios (obtained from the Australia-wide dataset).

Directed principal components [72] could help isolate the minor AlOH composition component from the dominant AlOH content component, though we also suggest using a color image (R:G:B) combination of red: B_7/B_6, green: B_7/B_5, and blue: B_7/B_6, with the intensity depicting the AlOH content and the hue (color) expressing the target AlOH composition, with kaolinite-rich pixels generating green tones and muscovite-rich pixels generating magenta tones.

Finally, the inverse relationship between the 2165 nm absorption depth (Equation (6)) and the 1900 nm water absorption depth (Equation (7)) ($R^2 = 0.37$, Table 1) is consistent with kaolinite having low affinity with water, unlike illite and, to a greater extent, montmorillonite, which absorb water molecules in their interlayers [73]. This relationship has previously been used to help separate illite (and muscovite) from montmorillonite [6].

3.6. Vegetation Unmixing Process

Figure 3 presents a suite of 2D scattergrams of various indices collected from the entire Australian ASTER dataset. The spatial coherency of these data clouds is a testament to the success of the L1T calibration [74] and cross-calibration [35] of >3000 ASTER images. These 2D scattergrams also show a variety of geometries. One type approaches an amorphous "blob" (Figure 3a,b,g,h), which indicates no apparent relationship between the input variables. The first two involve the water content ($(B_5 + B_8)/(B_7 + B_9)$), with the lack of a relationship with vegetation cover also evident in the associated imagery (Figure 4i). Thus, no vegetation unmixing is required for the ASTER's water content product. Having said this, the 2D scattergram of water content versus TIR-derived dry vegetation (Figure 3c) shows a "T" pattern involving two overlapping populations, neither of which is apparently correlated with the water content.

The AlOH content (Figures 3d,e and 4d) shows very different behavior to the water content (Figures 3a,b and 4i). The 2D scattergram of AlOH content versus green vegetation content (Figure 3c) approximates a right triangle (highlighted by a yellow line in Figure 3d), with its three apices representing (i) 100% green vegetation (0,1); (ii) 100% AlOH mineral content (1,0); and (iii) 0% of both (0,0). Given this "ideal" mixing geometry, the next step in the unmixing process (Equation (4)) involves transforming each pixel's estimation of its green vegetation content (examples shown by the white vectors) onto the AlOH content axis (Equation (4)). This transformation yields, as expected, an amorphous "blob" (Figure 3g).

Even more complex 2D geometries are expressed by the AlOH content versus the SWIR-derived and TIR-derived dry vegetation indices (Figure 3e and Figure 3f, respectively). Nevertheless, using Equation (4) to unmix the AlOH content using both of these dry vegetation indices results in (i) the SWIR-derived dry vegetation data cloud collapsing to a dimensionless blob (Figure 3g), while the TIR-derived dry vegetation data cloud increases its spread (in the direction of the white arrows in Figure 3i), and (ii) the associated unmixed images show suppression of fire scars (when comparing Figure 4d with Figure 4e,f). This indicates the "dry vegetation" indices using either the SWIR and TIR wavelength regions (Equations (2) and (3), respectively) are modeling essentially the same information. Thus, either dry vegetation algorithm (Equations (2) and (3)) can be used for the unmixing process (Equation (4)), though we suggest using the SWIR-derived index (Equation (2)) simply because it can be implemented at a 30 m pixel resolution in comparison to the 90 m pixel resolution of the TIR index. Note also the narrow zones of elevated response (black/white arrows in Figure 4), which are likely caused by residual mineral information in the dry vegetation indices (Figure 4b,c). These result in a neutral-colored (~white) response in the AlOH composition map (Figure 4h).

A comparison of Figure 4g versus Figure 4h shows the impact of vegetation unmixing on the AlOH composition product; that is, a coherent geological pattern is revealed after unmixing (Figure 4h), including most/all of the published paleo-geomorphic elements as well as clear demarcation of muscovite-rich "uplands" in the center and northwest and kaolinite-rich "lowlands" in the southeast, none of which is apparent in the non-unmixed products (Figure 4g). However, we emphasize the importance of gauging the appropriate gain levels (a and b in Equation (4)), which, in this case, were determined using visual criteria (suppression of fire scars) from only the area shown in Figure 4 and not at the continental-scale, which was the case for the other "unmixed" images shown in this paper; that is, the magnitude of these user-defined gains will impact the information clarity/accuracy of the unmixed products, so careful iteration and validation are critical.

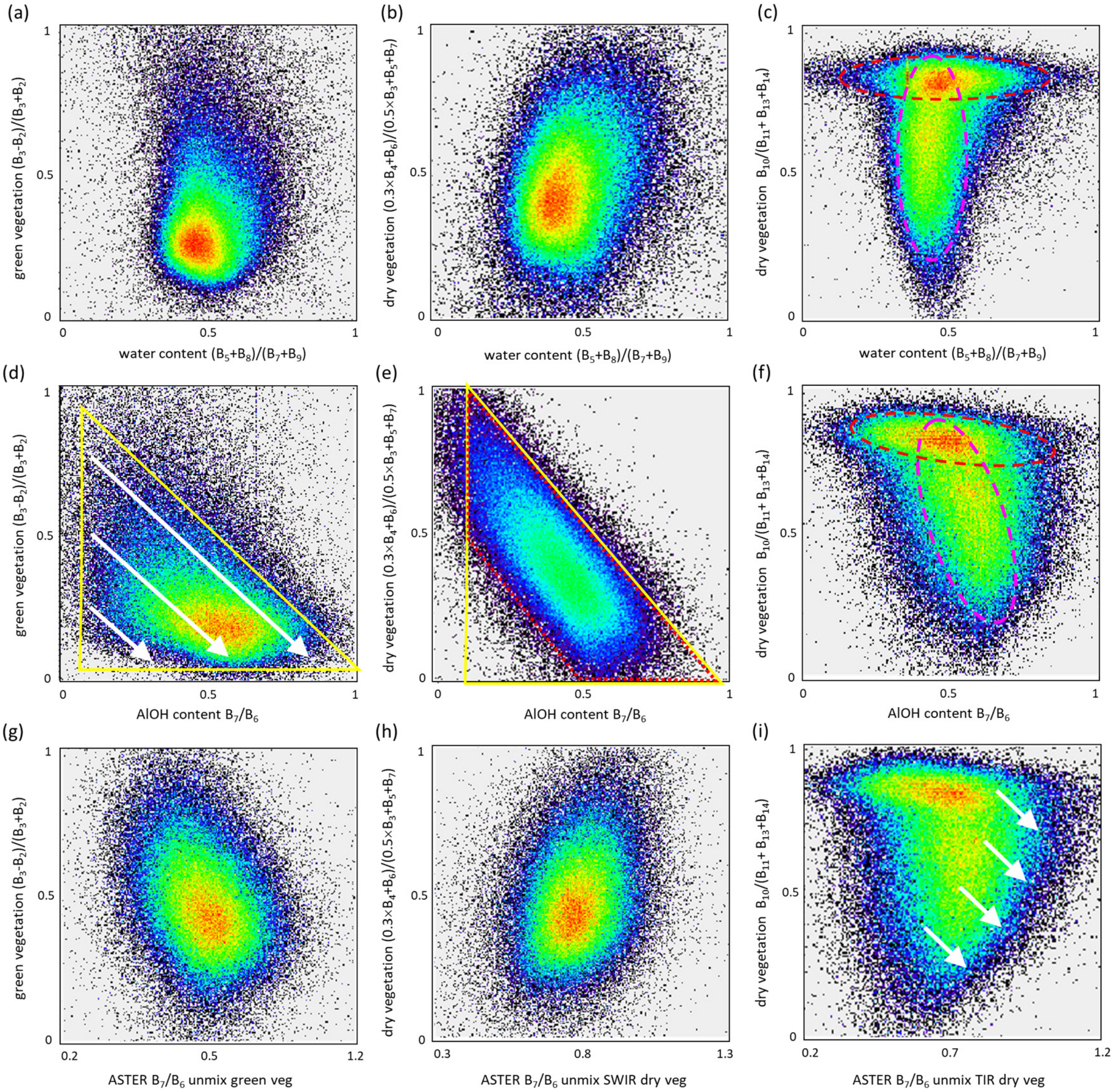

Figure 3. Two-dimensional scattergrams of the selected indices generated from the Australian ASTER mosaic data. (**a**) Water content vs. green vegetation. (**b**) Water content versus SWIR-derived dry vegetation. (**c**) Water content versus TIR-derived dry vegetation. (**d**) AlOH clay content vs. green vegetation. (**e**) AlOH clay content vs. SWIR-derived dry vegetation. (**f**) AlOH clay content vs. TIR-derived dry vegetation. (**g**) AlOH clay content after green vegetation unmixing vs. green vegetation. (**h**) AlOH clay content after SWIR-derived vegetation unmixing vs. SWIR-derived dry vegetation. (**i**) AlOH clay content after TIR-derived vegetation unmixing vs. TIR-derived dry vegetation.

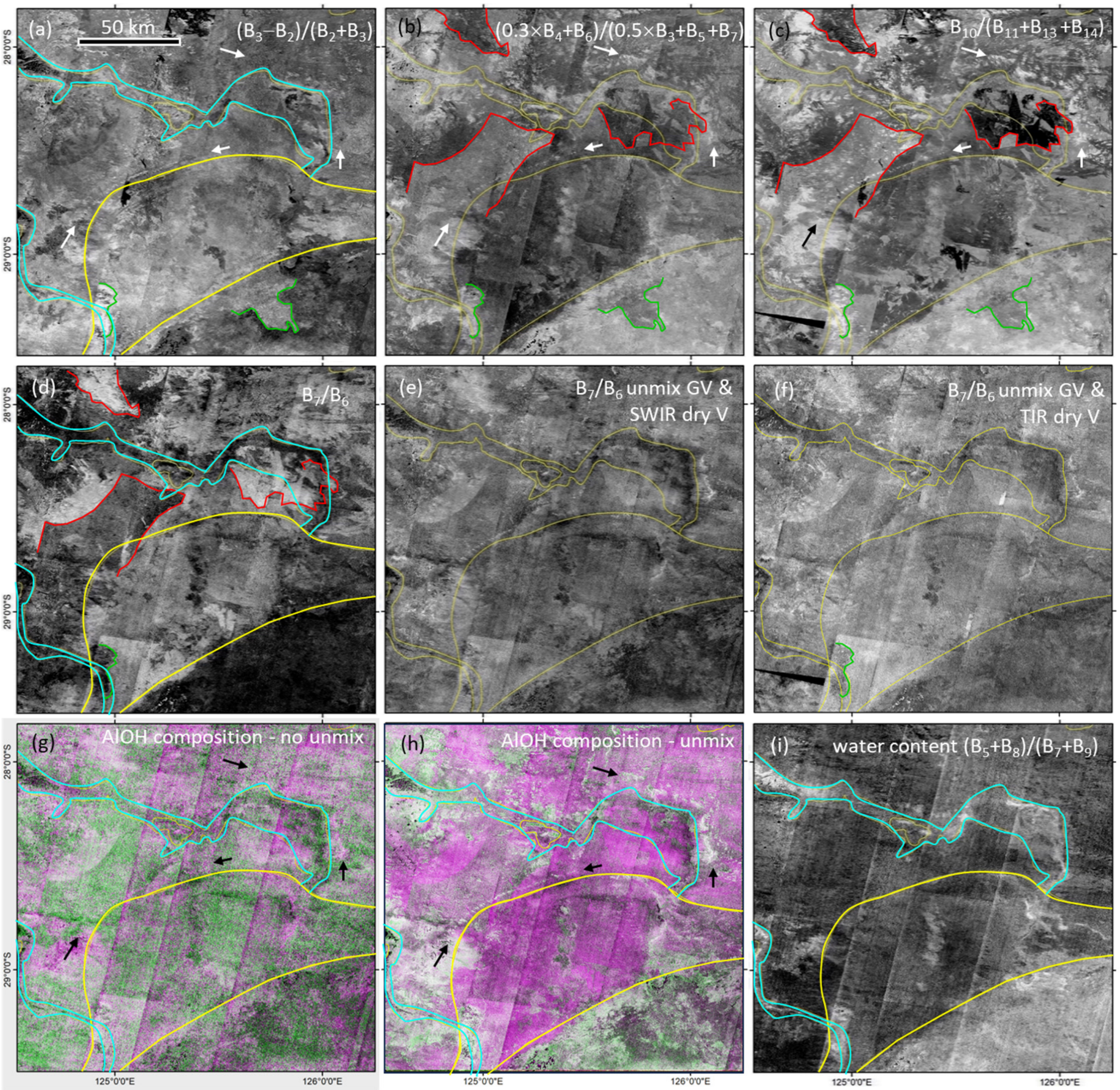

Figure 4. ASTER vegetation unmixing results for the same area shown in Figure 1. (**a**) Green vegetation (Equation (1)). (**b**) SWIR-derived dry vegetation content (Equation (2)). (**c**) TIR-derived dry vegetation content (Equation (3)). (**d**) AlOH content (B_7/B_6). (**e**) AlOH content unmixed of green and SWIR-derived dry vegetation. (**f**) AlOH content unmixed of green and TIR-derived dry vegetation. (**g**) AlOH composition (R:G:B—B_7/B_6: B_7/B_5: B_7/B_6) with no vegetation unmixing. (**h**) AlOH composition (B_7/B_6: B_7/B_5: B_7/B_6 as R:G:B) unmixed of green and SWIR-derived dry vegetation. (**i**) Water content ((B_5 + B_8)/(B_7 + B_9)) with no vegetation unmixing. Published [47] paleo-rivers are cyan, and paleo lagoons/shorelines are yellow polylines. White/black arrows highlight narrow zones of elevated response likely related to residual mineral information in both dry vegetation indices.

3.7. The Australian Continent ASTER Results

The impact of unmixing at the continental-scale is also pronounced. For example, unmixing the AlOH content (compare Figure 5a,b) shows overall increase across the >250 mm (magenta line) annual rainfall zone, which results in better agreement with the associated NGSA data (colored dots), e.g., areas like "B" and "C". The unmixing of the silica index (Figure 5e) yields similar increases across the >250 mm zone, including, for example, "D", which is associated with deep sandy soils and sand dunes of the Little Desert, which was not apparent in the original ASTER geoscience maps [5,6]. In arid areas (<250 mm rainfall), the AlOH content is reduced along the tract of the Darling River (highlighted by small yellow arrows) and for large parts of the Lake Eyre ("A") and Canning Basins (Figure 5b) but is elevated in the southern Yilgarn Craton (cyan polygon) and the rim of the Lake Eyre Basin ("A"), which coincides with opal deposits (red triangles).

The unmixed AlOH composition (Figure 5c) generates a different pattern compared with the original 2012 product [5,6]; for example (i) the northeastern Yilgarn Craton (dashed cyan polygon), Arunta–Musgrave complex (dashed white polygon), and Gawler Block (dashed yellow polygon), as well as the regolith between them, were originally mapped as dominantly kaolinite-rich but are now relatively muscovite-rich; (ii) the Eucla Basin, which was originally mapped as muscovite-rich [5], is now kaolinite-rich; (iii) the central part of the Lake Eyre basin ("A") is more kaolinite-rich; and (iv) the <250 mm rainfall zone is now largely muscovite-rich, while the >250 mm rainfall zone remains kaolinite-rich. The latter may reflect the high solubility/mobility of potassium [75]. Importantly, the NGSA kaolinite–muscovite spectral index (color-coded dots in Figure 5) better matches the updated results.

After unmixing, a N–S zonation becomes apparent especially in the western half of the continent across ~25° S latitude, with kaolinite developed in the north and abundant muscovite in the south (Figure 5b,d). This zonation is consistent with (i) the climate-driven high-pressure belt and associated prevailing wind pattern (yellow open arrows) [76]; (ii) relatively thin crust under the Canning and Lake Eyre Basins [77]; and (iii) the proposed Neogene "tilt axis" (black dashed line in Figure 5b), which is based on Cenozoic marine sediments being 250 m above the present-day sea level in the south while they are at present-day sea level in the north [78]. The vegetation unmixing also appears to better define the "Menzies Line" (yellow line in Figure 5b,d,f), which marks a transition from alkaline, fresh groundwater in the north (muscovite-rich) to acid, saline groundwater in the south (kaolinite-rich) [75,79,80].

The water content product (Figure 5f), which did not require vegetation unmixing, shows similarity with the NGSA 1900 nm absorption depth (similar color-coded dots), except for "wet" latitudes north of ~19° S, with some individual satellite tracks standing out, e.g., north of the Canning Basin. This seasonally "wet" region is likely caused by the timing of ASTER images being acquired during the wet-tropical summer to maximize the high sun angle. Across the arid zone (<250 mm), the ASTER water content largely follows the ASTER AlOH products (when comparing Figure 5f with Figure 5b,d), including a "wet" kaolinite-rich Eucla Basin and "dry" muscovite-rich regions of the Yilgarn, Gawler, and Arunta–Musgrave terranes. The Lake Eyre region ("A"), however, shows departure, e.g., "wet" muscovite east of "A", which likely reflects the development of a hygroscopic clay like montmorillonite instead of "muscovite" [6].

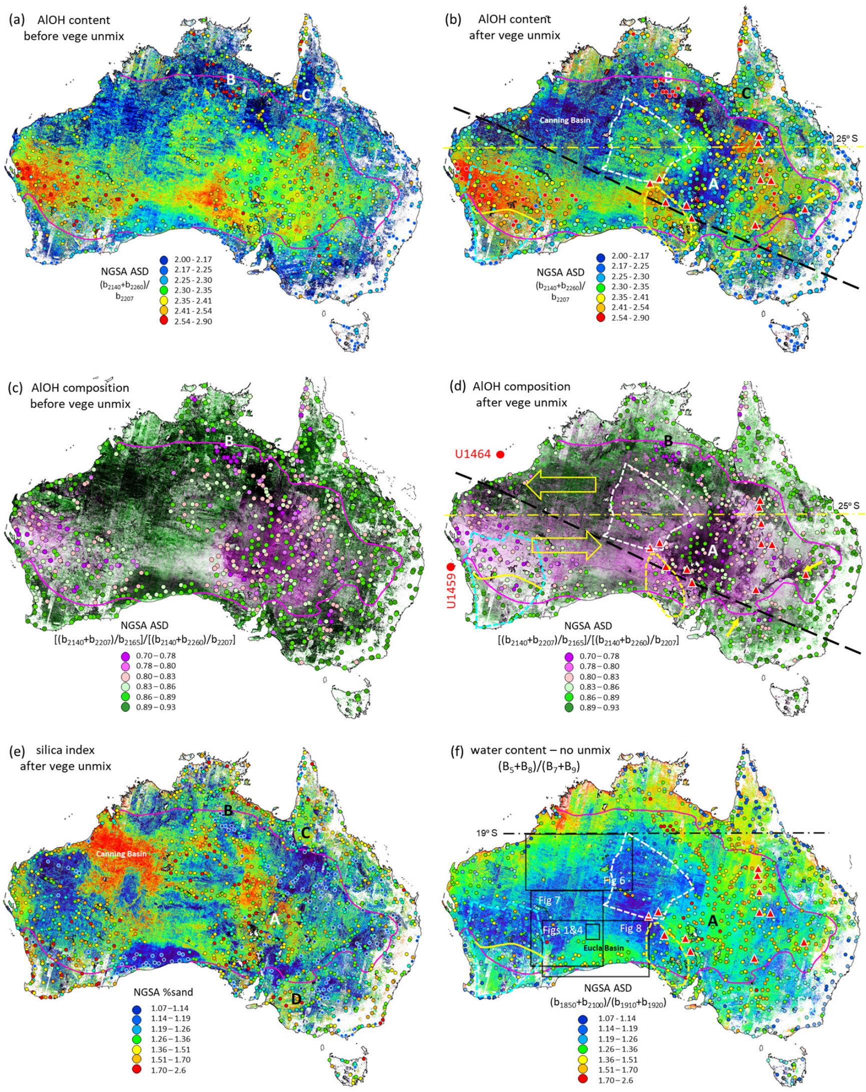

Figure 5. ASTER composition maps of Australia with comparable NGSA ASD validation data (colored dots). (**a**) ASTER AlOH content (B_7/B_6) map before green and dry (TIR) vegetation unmixing. (**b**) ASTER AlOH content (B_7/B_6) map after green and dry vegetation mixing. (**c**) ASTER clay composition (B_7/B_5) map before green and dry vegetation unmixing. Magenta tones indicate muscovite, while green tones indicate kaolinite. Intensity is related to the 2200 nm absorption depth, with brighter shades related to abundant dioctahedral clay mineral content (see Figure 2b). (**d**) ASTER clay composition (B_7/B_5) map of Australia after green and dry (TIR) vegetation unmixing. (**e**) The ASTER silica index ($B_{13}/(B_{10} + B_{11} + B_{12})$) after green and dry vegetation unmixing. (**f**) ASTER water content $(B_5 + B_8)/(B_7 + B_9)$ product (Table 1) masked for green vegetation only. All maps have been masked to remove to the top ~10% of pixels with abundant green. NGSA validation data embedded as colored dots. The magenta line is the annual 250 mm rainfall isohyet [48]. The dashed, cyan, white, and yellow polygons show the Yilgarn, Arunta–Musgrave, and Gawler Blocks, respectively. Yellow arrows highlight the Darling River. The yellow line marks the "Menzies Line" [79]. Red triangles show the major opal deposit fields. Red dots (with labels) are sites of the ocean drilling program (ODP) [76]. The black dashed line is a proposed Neogene "approximate tilt axis" [80]. A to D are locations referred to in the body text.

3.8. Paleo-Valleys of the Canning Basin Region

The Paleozoic Canning Basin [81,82] in northern Western Australia (Figures 5f and 6) was superimposed by a network of paleo-valleys [41,47,83] (Figure 6a) before superposition by aeolian quartz sands of the Great Sandy, Little Sandy, Tanami, and Gibson Deserts. This quartz sand cover is well-mapped using the (vegetation unmixed) ASTER silica index (warmer colors in Figure 6b). The present land surface is also obscured by a patina of fire scars, which is evident in both the ASTER false color composite (Figure 6a) and non-unmixed AlOH content (Figure 6c) products. After vegetation unmixing, the AlOH content (Figure 6d) clearly reveals this paleo-river network (Figure 6a), including fine-scale paleo-valleys, such as those near "E". Many of these paleo-valleys are mapped "under" aeolian sand cover (e.g., "G" in Figure 6b), being characterized with a low AlOH content, similar to the present-day Darling River (yellow arrows in Figure 5b).

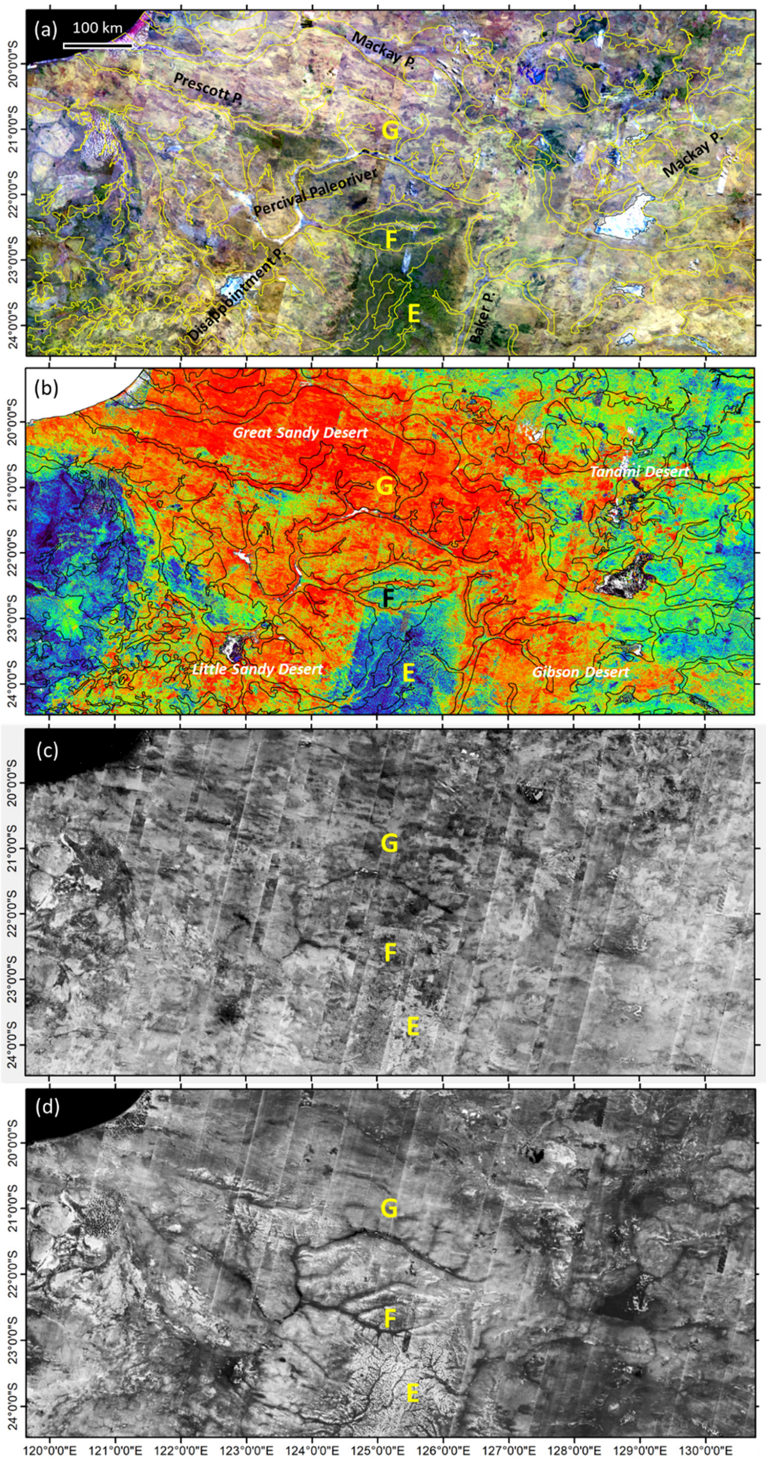

Figure 6. ASTER mosaics of the Caning Basin, Western Australia. (**a**) False color (R:G:B; ASTER band 3: band 2: band 1) with published paleo-rivers [47]. (**b**) Silica index ($B_{13}/(B_{10} + B_{11} + B_{12})$ with vegetation

unmixing. Warmer colors are associated with quartz-rich sands. The names of the sand deserts are shown. (**c**) The 2012 AlOH content ((B_5 + B_7)/B_6)) without vegetation unmixing. (**d**) The 2012 AlOH content ((B_5 + B_7)/B_6)) with vegetation unmixing. Brighter tones in the gray-scale images equate to greater (apparent) amounts of AlOH mineral content. E to G are locations referred to in the body text.

The possible causes of this low AlOH content associated with river channels (Figures 5b and 6d) include (i) mobile, "platy" AlOH-bearing minerals (e.g., muscovite) being preferentially removed by (paleo) flood events; and/or (ii) AlOH-poor sand and/or heavy mineral grains preferentially accumulating in valley lows and effecting the optical depth of the spectral measurement [67,84,85]. The reason why paleo-valleys are mappable using the ASTER across the entire Canning Basin, irrespective of the aeolian sand cover, may be related to the role of the swales between the sand dune ridges exposing underlying AlOH mineralogy.

3.9. Paleo-Valleys of the Eastern Yilgarn Craton Region

The Cenozoic paleo-valleys in the southeast region of Western Australia (Figures 5f and 7b) once transported sediment that was eroded from a variety of bedrock geologies (Figure 7a) [86], including (i) Archaean granite–greenstone belts of the Yilgarn Block (cyan polygon in Figure 6); (ii) Archaean-to-Proterozoic high-grade metamorphic rocks of the Albany-Fraser Orogen; (iii) a series of Proterozoic to Cambrian basins of largely siliciclastic sediments; (iv) Carboniferous to Permian glaciogenic sediments of the Canning Basin; and (v) Cretaceous siltstones and sandstones of the Gunbarrel Basin (Figure 7a). The Neoproterozoic to Late Devonian Officer Basin underlies the Carboniferous to Cretaceous sequences in this area [87]. Today, the paleo-rivers are expressed over low relief (~600 m vertical change over ~600 km distance) (Figure 7b) [88,89] and include: (i) eastward flowing systems like the Carey, Raeside, Yindarlgooda, and Lefroy Paleorivers, with catchments spanning Archaean rocks of the Yilgarn Block and Proterozoic rocks of the Albany-Fraser Orogen; and (ii) southward flowing systems like the Throssel and Baker Paleorivers, with catchments spanning Phanerozoic rocks to the north. That is, this region contrasts with the Canning Basin area (Figure 6) as it comprises diverse, "upland" (exposed and erosional) geological environments.

Similar to the Canning Basin results (Figure 6c,d), vegetation unmixing is effective in suppressing fire scars, as shown by a comparison of the before/after AlOH content products (Figure 7d,e). However, this unmixing reveals a change from higher AlOH contents and muscovite-rich in the south to lower AlOH contents and kaolinite-rich in the north (Figure 7e,g), consistent with the continental-scale results (Figure 5b,d). This change occurs over a narrow (~100 km wide) zone (white dashed line in Figure 7d,g) that crosscuts the Phanerozoic geology (Figure 7a) and landform (Figure 7b) and is not apparent in any other ASTER (Figure 7f,h) or geophysical products (Figure 7c); that is, it is specifically an AlOH mineral signature.

The ASTER AlOH composition map (Figure 7g) shows the surface of the Yilgarn Block (Figure 7a) to be muscovite-rich, which is consistent with the high K response in the airborne gamma radiometric image (Figure 7c). However, this compositional association is not universal. For example, a pronounced high K radiometric response of the Eucla Basin, as well as smaller K-rich areas over "upland" rocks (highlighted by dashed-yellow polygons in Figure 7c), are relatively kaolinitic in the ASTER AlOH composition product (Figure 7c,g). This apparent inconsistency between sensing techniques can be explained by (i) the K-bearing minerals being feldspars, such as microcline ($KAlSi_3O_8$) or orthoclase ($KAlSi_3O_8$), and not an AlOH-bearing phyllosilicate, like muscovite; or (ii) the different sensing penetration depths. That is, gamma rays can persist through a meter of dry, porous, bare ground [90], while "optical" sensing penetrates the top few microns [84,91]. For example, a thin kaolinite-rich weathering rind developed on a microcline-bearing rock.

In contrast with the Canning Basin (Figure 5d), the composition of paleo-drainage across this diverse, (paleo-)erosional geological environment (Figure 7) is expressed as low AlOH content for only some, intermittent segments of paleo-valleys and only for some types of exposed bedrock, such as those parts arrowed off "K" over the Yilgarn Craton (Figure 7e). However, even over this bedrock type, the surface composition of paleo-valleys alternates (10–100 km) between (i) low AlOH content, kaolinite-rich, low quartz sand content, high water content, high opaque content (Figure 7e, 7f, 7g, 7h, and 7i, respectively), and high ASTER gypsum content [86], for example, "K" and "L", and (ii) high AlOH content, high quartz sand content, muscovite-rich, low water content, low ASTER opaque content [86] (Figure 7e, 7f, 7g, 7h, and 7i, respectively), and low ASTER gypsum content [86]; for example, "H". The latter type seamlessly merges with the surrounding "upslope" geology/regolith. This alternating pattern indicates that a number of factors have driven the surface composition of paleo-valleys. One possibility is groundwater condition, especially as this area represents the transition across the "Menzies Line" [75,79]; that is, (i) above is related to shallow, acidic groundwater, while (ii) above is related to deeper and/or neutral groundwater. Unfortunately, there are too few groundwater sample points [92,93] to corroborate an association between groundwater chemistry and surface mineral composition.

Over the Carboniferous–Permian and Cretaceous rocks (Figure 7a), paleo-valleys are more consistently richer in quartz sand content (Figure 7f), though this signature merges/broadens downslope into similarly high responses over the aeolian sand plains/dunes of the Gibson and Great Victoria Deserts (Figure 7b,f). The pattern of quartz-sand-filled paleo-valleys over the Phanerozoic rocks both mirrors and helps explain the low gamma-radiometric response (Figure 7c).

The alternating compositional pattern of paleo-valleys across the Yilgarn Craton (Figure 7) terminates against a ~150 km wide, 600 km long, NW–SE-trending "dry" zone (red polygon in Figure 7g). Note that this "dry" zone is not an atmospheric effect nor caused by recent rainfall because it is measurable over dozens of ASTER scenes collected over many years, and most importantly, it aligns with the surface mineralogy, including a lack of opaque minerals (Figure 7i) and gypsum [86], as well as a dearth of hydrothermal gold deposits (Figure 7i). Down-stream from this "dry" zone, the paleo-valleys return to being "wet", AlOH-poor, kaolinitic, gypsiferous, and rich in opaque minerals (e.g., "N").

This "dry" zone (red polygon in Figure 7h) also coincides with a zone of higher deformation (i.e., tectonic thrust stacking) and increased granite intrusions, as interpreted from the 2001 seismic (01AGS-NY1 black dashed line in Figure 7i) and gravity data [94]. There is also a related paucity of gold-associated greenstone keels [95] (green units in Figure 7a). There is another, albeit smaller/weaker, "dry" zone further to the east (red dashed line in Figure 7h), which, from the seismic and (11GA-YO1) drill-hole (DH) data [95] (DH) [95,96] (magenta triangles in Figure 7i), corresponds to a rapid, west-to-east thickening of the Phanerozoic cover stratigraphy from the Empress DH (~500–1500 m) to Yowalga DH (>4100 m depth). The thinner western part of this zone is developed over a strongly reflective middle crust and a gravity high [95]. Thus, the surface "dry" zones mapped using the ASTER have deeper crustal associations that appear to persist through sedimentary/regolith cover. Ideally, these ASTER results should be combined with drill-core data [97] to better map/understand the 3D architecture.

The updated ASTER mineral maps (Figure 7) also provide new information about the Eucla Basin, much of which appears to cross-cut the published Eocene depositional features (blue dotted, dashed, and solid lines in Figure 7b) [47,50] that host heavy mineral sand occurrences (green dots) [54]. These new features include (i) a possible barrier shoreline ("M", which is highlighted by a black dotted line) characterized by a linear edge/zone of elevated quartz sand (Figure 7f) and AlOH content (Figure 7e) rich in muscovite (Figure 7g); (ii) a possible back-beach lagoon ("J") characterized by low quartz sand and AlOH contents and is relatively rich in kaolinite as well as comprising an apparent meandering (paleo) channel ("O" in Figure 7b) that extends southward from the mouth of Throssel Paleoriver and terminating at the barrier shoreline "M"; and (iii) a multi-lobate, deltaic-like fan ("I") outboard of the mouth of the Carey Paleoriver that comprises elevated quartz sand and AlOH contents and is muscovite-rich. These, and other depositional features across the Eucla Basin, are described in more detail below.

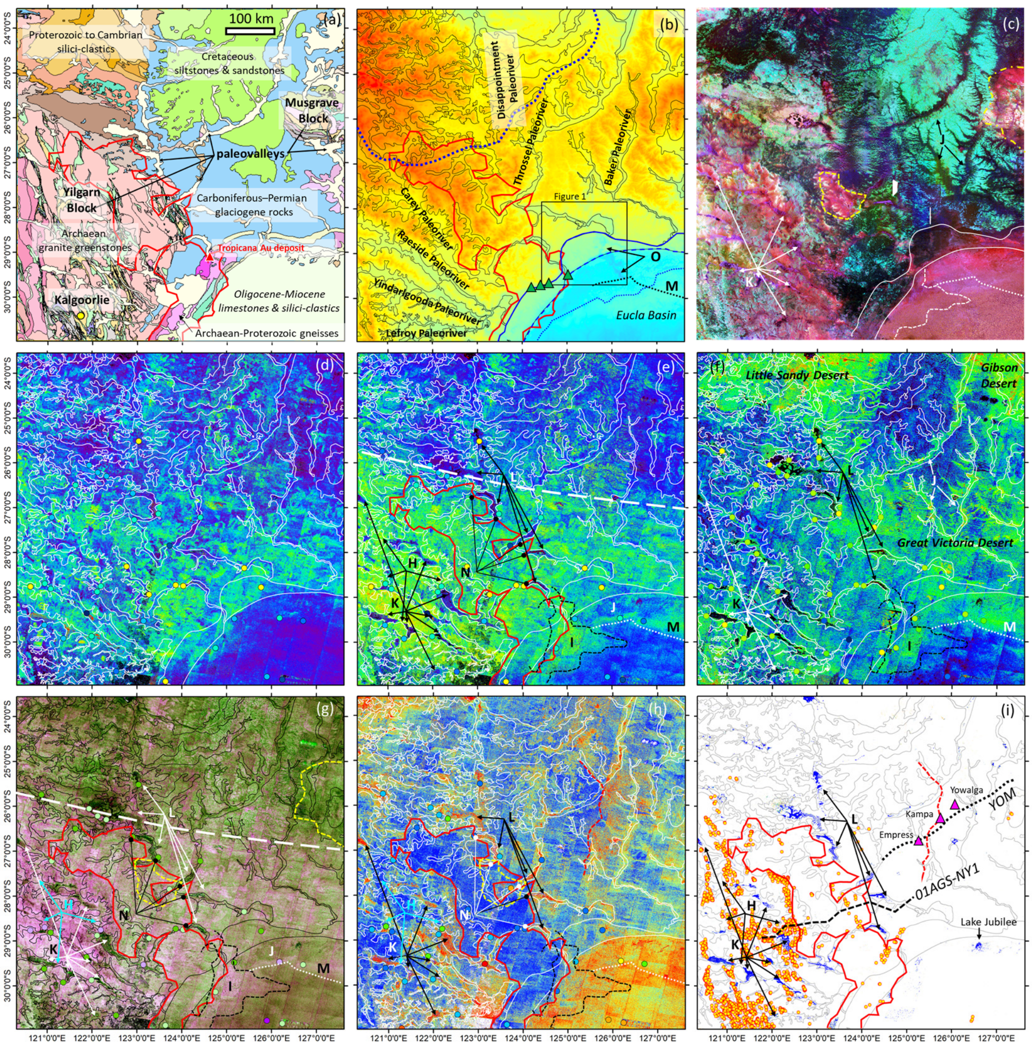

Figure 7. Various geoscience maps of southeast Western Australia (see Figure 5f for location). (**a**) 1:2,500,000-scale bedrock geology overlain with 1:2,500,000-scale Cenozoic geology [86]. (**b**) GEODATA 9 Second digital elevation model [51] overlain with the 2012 WASANT paleo-valley map in gray lines. Strandlines: Middle Eocene—dotted blue line; middle-late Eocene (and Miocene?)—solid blue line; late Eocene—dashed blue line [98]. (**c**) Airborne gamma radiometric total count image (R:G:B; K:Th:U) [53]. (**d**) ASTER 2200 nm absorption depth ratio, B_7/B_6, with no vegetation unmixing. Warmer colors represent greater abundance. (**e**) ASTER 2200 nm absorption depth ratio, B_7/B_6, with vegetation unmixing. White dashed line marks the approximate boundary between low and high AlOH content. (**f**) ASTER silica index ($B_{10}/(B_{11} + B_{12} + B_{13})$) map [21] with vegetation unmixing. (**g**) ASTER clay composition map based on B_7/B_6 and B_7/B_5 with vegetation unmixing. Magenta tones are muscovite, while green tones are kaolinite. (**h**) ASTER water content index ($(B_5 + B_8)/(B_7 + B_9)$), with cooler tones relating to low water content. (**i**) ASTER opaque index (B_4/B_1) [5,86], with the threshold set to only show those areas rich in spectrally-flat materials. Yellow dots with red rims are gold occurrences/deposits [86]. Two seismic lines [95,99] are shown as black dotted/dashed lines. Small colored dots are NGSA sample data [36–38], including: (**d**,**e**) AlOH content (B_7/B_6); (**f**) Si/(Si + Al); (**g**) $((b_{2140} + b_{2207})/b_{2165})/((b_{2140} + b_{2260})/b_{2207})$; and (**h**) $(B_5 + B_8)/(B_7 + B_9)$. H to O are locations referred to in the body text.

3.10. Miocene Littoral Deposits across the Eucla Basin

The published geology of the Eucla Basin [50,81,82,86,100–106] includes (i) Eocene barrier shoreline/lagoon systems (Figure 8a); (ii) Oligocene-to-Miocene limestones and sandstones; and (iii) quaternary sands, with the major marine regression occurring in the middle-to-late Miocene as the climate cooled and aridity increased. The early-to-mid-Miocene, ~30 m thick Nullarbor Limestone grades northward into the fossiliferous Colville Sandstone, which is <23 m thick and up to 120 km wide (the published "approximate" boundary [105] is shown by the orange line in Figure 8b–d). The Colville Sandstone comprises thin-interbedded, micaceous sandstones, sandy calcarenites, shales, siltstones, and conglomerates, which were deposited on the margin a marine shelf (30–45 m depth) characterized by good circulation. In the eastern part of the Eucla Basin, the thinner Yarle Sandstone (<10 km wide) is a silicified and ferruginous sandstone unit containing rare clasts of Nullarbor Limestone (as well as fossils) that were deposited along a moderate-energy beach strandline. These early–mid-Miocene Eucla-group rocks became emergent (and remain so to this day) by the Pliocene, driven by global cooling (falling sea level) and tectonic uplift (at 8–9 Ma) across southern Australia [50,78].

The mapping of the mid- and late-Eocene shorelines across the Eucla Basin is well-established [47] (Figure 8a), though mapping the Miocene shoreline/s, especially the Colville Sandstone, has been more of a challenge [50]. In the field, the Colville Sandstone is distinguishable by a surface pediment rich in quartz sand variably covered by mulga woodlands. This changes southward to myall scrub developed over calcareous soils associated with the Nullarbor Limestone [100]. Another challenge is unravelling the relationship between the contemporaneous (?) Miocene Colville and Yarle Sandstones.

These issues are targeted here using the ASTER products: (i) water content (Figure 8a); (ii) silica index (Figure 8b); (iii) AlOH content (Figure 8c); (iv) AlOH composition (Figure 8d); and (v) the carbonate index (B_{13}/B_{14}) [107]. Note that the ASTER carbonate index image is not presented in Figure 8 because it is visually compromised by image-to-image miscalibration errors largely caused by uncorrected water vapor [5]. It nonetheless has sufficient "mineralogical" contrast to define the approximate boundary between regions of high versus low carbonate contents, with this boundary shown as a white dashed line in Figure 8b–d. Importantly, all of the ASTER products presented in Figure 8 show close similarity with their respective field validation NGSA measurements (colored dots), underlying the reliability of the geoscience information available from these new ASTER products but not present in the original 2012 ASTER products [5].

The water content image (Figure 8a) shows large (~500 km wide), coherent domains, including: (i) a relatively "wet" (=warmer tones) Eucla Basin; (ii) moderate water contents across the mid-Eocene barrier-beach lagoon zone, except for southwest of the Carey Paleoriver, where it is "dry"; (iii) moderate levels over much of the Phanerozoic cover rocks, to the north, including over the Officer Basin; and (iii) "dry" (=cooler tones) zones over parts of the Yilgarn Block and Albany-Fraser Mobile Zone in the west (discussed previously) and the Gawler Craton in the east (red lines). Anomalously "wet" satellite overpasses produce step effects, e.g., green arrows, which were likely caused by rainfall occurring shortly before image acquisition. Ideally, the affected images should be replaced in the National ASTER mosaic with "drier" images.

The uniformly "wet" ASTER signature of the Miocene Eucla Basin (Figure 8a) is cross-cut by a pattern of quartz sand in the north versus carbonate in the south (Figure 8b), with the boundary between these largely coincident, except near (i) "P", where there is a ~100 km wide area of elevated carbonate and silica contents, and (ii) "S", which is an alluvial fan/lobe-like feature off a paleo-river mouth to the west. This lobe also shows an apparent image/track calibration error (yellow arrows in Figure 8b) but is evident in the ASTER TIR module only. That is, this TIR mis-calibration also likely impacts the carbonate index but not the SWIR mineral information (Figure 8c,d). The pattern of AlOH content (Figure 8c) cross-cuts the "wet" AlOH signature of the Eucla Basin (Figure 8a) and broadly coincides with high silica content, though it also shows opposite patterns, e.g., "Q" and "R".

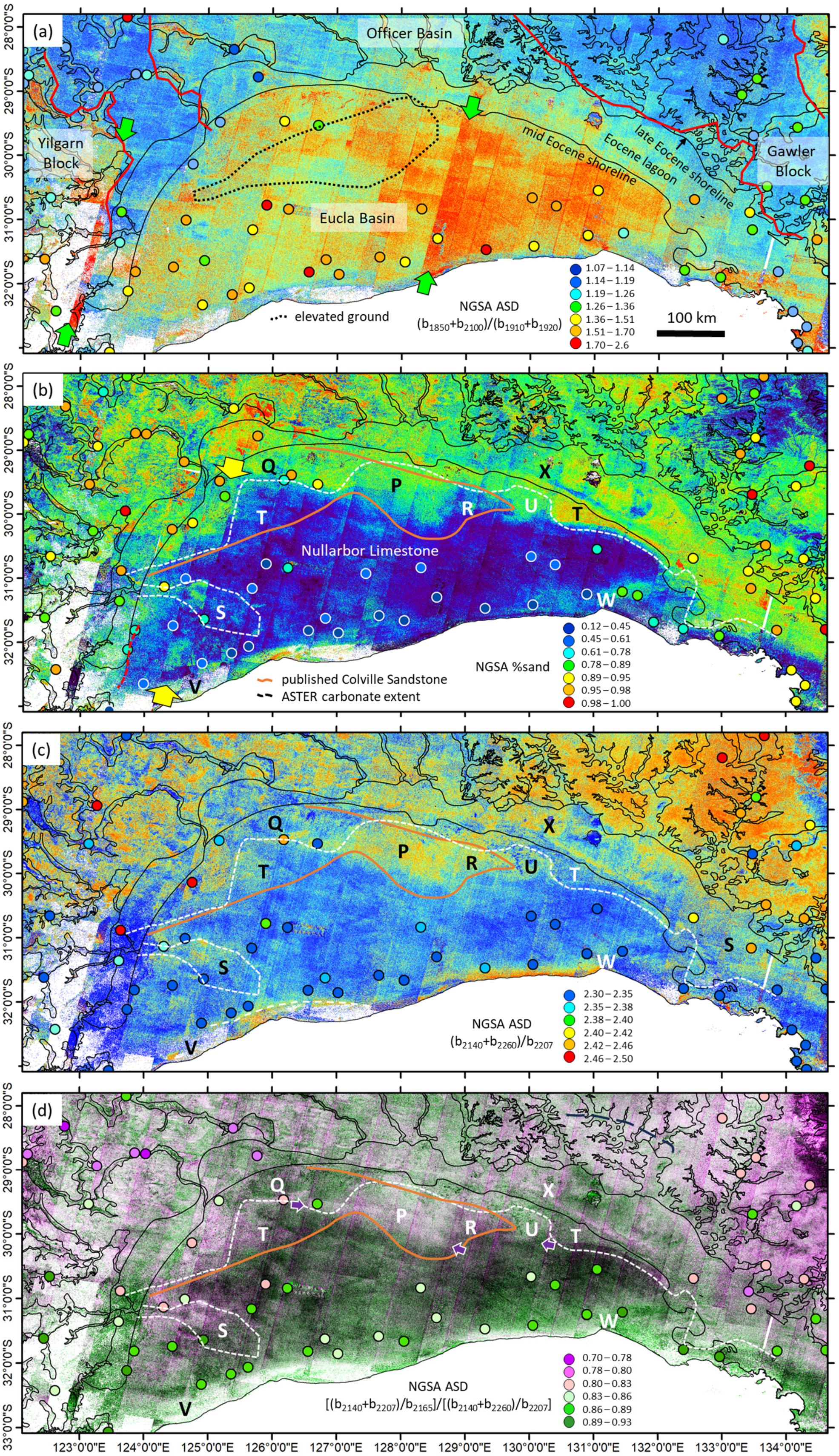

Figure 8. Eucla Basin ASTER composition maps. (**a**) ASTER water content index $((B_5 + B_8)/(B_7 + B_9))$ image with the validation NGSA ASD 1900 nm absorption depth as colored dots. Green arrows show satellite tracks collected over "wet" (recent rainfall) ground. Red lines are (stable) low water content

zones. The black dotted polygon is the approximate limit of a 60 m high topographic rise, as evident in the DEM [51]. (**b**) Vegetation unmixed ASTER silica index, with the validation NGSA %sand as colored dots. Yellow arrows highlight a probable image/track calibration error. (**c**) Vegetation unmixed ASTER AlOH content with the validation NGSA ASD $((b_{2140} + b_{2260})/b_{2207})$ index shown as colored dots. (**d**) Vegetation unmixed ASTER AlOH composition with the validation NGSA ASD $((b_{2140} + b_{2207})/b_{2165})/((b_{2140} + b_{2260})/b_{2207})$ index shown as colored dots. The white dashed line marks the (northern) edge of high ASTER carbonate index values. A published [105] extent of the Colville Sandstone is shown by an orange line. P to X are locations referred to in the body text.

Based on the ASTER maps (Figure 8b–d), the Yarle Sandstone ("T") is characterized by (i) a high silica index, i.e., high quartz sand content; (ii) a low carbonate content; (iii) a low AlOH content; and (iv) is kaolinitic. The Yarle Sandstone ("T") exhibits a pronounced north–south gradient in the silica index (Figure 8b) and has a geometry that is relatively smooth, curvilinear, and westward-widening, terminating close to the carbonate index transition (white dashed line) between U and T. These characteristics contrast with the Colville Sandstone (spans "Q", "P" and "R") which is characterized by (i) moderate levels of quartz sand content; (ii) variable carbonate content; (iii) generally high AlOH content; (iv) is generally muscovite-rich; and (v) cross-cuts the carbonate index transition. The Colville Sandstone also shows a different pattern of relatively diffuse N–S and E–W compositional gradients/boundaries, as well as a series of E–W linear, muscovite-rich zones (purple arrows in Figure 8c).

Based on this new ASTER information (Figure 8), we argue that the Miocene Yarle and Colville Sandstone units formed at different times and under different geomorphic/tectonic/climatic conditions (discussed in more detail below).

4. Discussion

The results above show that more accurate geoscience information is generated from the Australian ASTER reflectance/emissivity mosaic when vegetation unmixing is applied to affected products (Figures 1 and 4–8). These "affected" products are driven by the wavelength regions used for the mineral indices and whether these overlap with either green or dry vegetation spectral features; that is, where the vegetation is effectively "aspectral", it has no apparent effect on the mineral index. Thus, the SWIR and TIR mineral indices (e.g., the ASTER AlOH and silica indices, respectively) are prone to dry vegetation effects, while the VNIR mineral indices (e.g., iron oxyhydroxides) are prone to green vegetation effects.

Although estimation of the dry vegetation content using ASTER remains problematic, which is a consequence of the lack of diagnostic cellulose/lignin spectral bands, the SWIR- and TIR-based indices tested here (Equations (2) and (3)) were nevertheless effective in suppressing regional rainfall (Figure 5) and local fire scar (Figures 4, 6 and 7) vegetation patterns. Having said this, the method tested here is subjective, requiring the user to determine the "optimum" gains in Equation (4). Arguably, a more objective "Model Optimization Process", as part of an automated "Machine Learning" strategy, that corrects for both regional, climate-driven and local, fire-scare-driven vegetation patterns is required.

The few updated ASTER compositional maps presented here show that new and more accurate surface mineralogy is generated and that much of this information is not apparent from other "traditional" mapping data. This new mineral information includes (i) the extent/nature of the Colville Sandstone (Figure 7), with implications for heavy mineral sand exploration; (ii) a continental-scale N–S change in AlOH content/composition, which likely reflects a change in aeolian sediment transport controlled by the high-pressure belt at ~25° S (Figure 5b,d); (iii) "dry" zones (Figures 7h and 8a) that are anti-correlated with Archaean gold deposits and consistent with "buried" tectonic-structural zones; and (iv) a 1000 km wide, circular, muscovite-rich feature spatially associated with opal deposits (Figure 5b,d). Much of this new geological information should be examined in greater detail in future work, ideally in combination with spectral measurements (ASTER-simulated) of drill cores [98] as well as other (updated) ASTER mineral maps to generate a 3D perspective of the mineral/geologic architecture of specific mineral systems.

The results presented here show that the surface mineralogical expression of paleo-valleys and their catchments is complex, being dependent on terrane, geological exposure, groundwater, and aeolian processes. The apparent contrast in complexity between different upland/lowland terranes (Figure 6 versus Figure 7, respectively) also helps explain the "cold" signature of paleo-valleys often observed in night-time thermal infrared imagery [41,50,89]. That is, the detected cold signature in TIR kinetic temperature imagery is likely a cold air drainage "landform" effect rather than evaporative cooling of groundwater or a volumetric, thermal inertia effect, though either could be critical where the landform is clearly not the driver, e.g., ref. [108].

Here, we discuss in more detail how the updated ASTER maps can be interpreted to unravel the Miocene depositional history across the Eucla Basin [50]. The first stage is defined by the northern limit of carbonate development associated with the deposition of the Nullarbor Limestone, which we suggest is mappable using the ASTER carbonate index (black dashed line in Figure 9a). At this time, the bulk of the terrigenous sediment entering the marine basin was sourced from the northeast, presumably driven by localized tectonic uplifts [78]), and carried by the Meramangye Paleoriver (thick red arrow), as well as other rivers from the north (thin red arrows). Even though most of the eroding catchments were rich in quartz and muscovite (Figure 8b–d), the transported AlOH mineral component was either deposited in a low-energy environment before reaching the shoreline, such as a back-beach lagoon (e.g., X in Figure 8c), or separated from the quartz sand component in the high-energy shoreline environment before being transported by easterly longshore drift to be deposited further to the east. This resulted in the Yarle Sandstone being quartz sand-rich but AlOH-poor, with the bulk of this coarser sediment preferentially deposited near the mouth of the Meramangye Paleoriver ("T" in Figure 8).

The second stage (Figure 9b) involved a westward shift in the area of upland tectonic uplift [50,78,89] during a continuing marine regression, possibly also involving a pronounced "step-down" event in sea level caused by the tectonic activity. This resulted in the deactivation of the Yarle shoreline system and the initiation (expansion) of the Colville shoreline system, which operated both westward and southward of the previous axis of Yarle long-shore drift (Figure 9a). This also marked a change from a higher-energy, quartz sand-dominated shoreline to a lower-energy, AlOH–mineral-dominated shoreline, with the latter characterized by (i) a west-to-east gradient from quartz sand-rich (eastern limit shown by the orange line) to AlOH-rich (purple and green shading), which presumably reflects distance from the primary sediment source, direction of longshore drift and the particle size/shape of transported mineral grains; and (ii) a southward progradation of the shoreline, characterized by linear, muscovite-rich zones that intersect/start in the west and spread and fade eastward (e.g., purple arrows in Figure 8d). The Carey Paleoriver and, to a lesser degree, the Baker Paleoriver (magenta arrows in Figure 9) delivered much of this muscovite-rich sediment, while the Throssel, Wanna, and Noorina Paleorivers delivered kaolinite-rich sediments (green arrows in Figure 9b).

The third and final stage (Figure 9c) was associated with a continuing westward shift in tectonic uplift, now centered over the Yilgarn Block (Figure 5b,d), as well as more localized uplift, such as that over the basement block bounded by the Rodona and Mundrabilla Shear zones [109–112] (black dotted line in Figure 9d), which resulted in the emergence of the Bunda Plateau (blue dot-dashed polygon in Figure 9c). A suite of faults (yellow lines in Figure 9d) and rotated blocks [111,112] are also evidence of this uplift.

This localized uplift is expressed in the gamma radiometric signal (Figure 9d). That is, lower gamma radiometric signal generally corresponds to higher ASTER AlOH content (compare Figures 8c and 9d) associated with alluvial fans (e.g., "S" and "T"), which extend for ~200 km to the edge of the uplifted "basement" block (black dotted line), with the AlOH composition of each fan reflecting its sedimentary provenance. For example, the Throssel Paleoriver ("Q") delivered kaolinite-rich sediments (green arrow and green shading) from Phanerozoic cover rocks (Figure 7g), whereas paleo-rivers to the south (e.g., Carey Paleoriver "T") delivered muscovite-rich sediments (magenta arrows and magenta shading) from the Yilgarn Craton (Figure 7g).

This third phase of sedimentation was likely contemporaneous with a pulse of late-Miocene K-rich terrigenous sediments identified [76] in ocean drill core sediments (DH U1459 in Figure 5d) on the western side of the Yilgarn Craton. This K-rich (muscovite-rich) ocean sediment was proposed by the authors of [76] to be caused by increased rainfall over the Yilgarn Craton driven by a brief northward migration in the Miocene of the high-pressure belt. However, we suggest that the Miocene K-rich ocean sediment recorded at U1459 (Figure 5d) is the result of the activation of fluvial systems across the Yilgarn Craton caused by westward-intensifying, tectonic uplift across a continental-scale "hinge-line" (black dashed line in Figure 5) [78]. At any rate, the high-pressure belt is (again?) today located at ~25° S (yellow dot-dashed line in Figure 5), generating opposing E–W wind patterns (yellow arrows in Figure 5d) that, respectively, transport aeolian AlOH-rich sediments across Australia (Figure 5d) and into the neighboring marine environments [6,113,114]. That is, a flow of kaolin-rich aeolian sediment westwards in the north and muscovite aeolian sediment eastwards in the south (large open yellow arrows in Figure 5d), which are clearly mappable using the updated ASTER AlOH mineral maps (Figures 5d and 7e,g).

Given that the "Colville" shoreline mapped using the ASTER (Figures 8 and 9b) is correct, this presents a targeting opportunity for heavy mineral sand exploration across the central part of the Eucla Basin, especially given that Miocene age deposits (reworkings of Eocene deposits) have been identified [97,115] on the margins of the basin (red triangles in Figure 9b). The Yilgarn Craton source rocks of these interpreted Miocene shorelines are particularly attractive, given that world-class heavy mineral sand deposits on the west coast of Australia also sourced their economic endowment from the Yilgarn Craton. However, the interpreted low-energy nature of the "Colville" shoreline potentially limits the significance of this opportunity.

Finally, the updated Australian ASTER products presented here clearly show new geoscience information not apparent in other public mapping datasets. Even though this unique mineral information is sensed from only the top few microns, its complexity speaks of a multiplicity of processes that, in theory, can be untangled to generate potentially unexpected information about our Earth system, such as that shown here for the Miocene geomorphic history of the Eucla Basin. Importantly, the methods and maps presented in this paper are a significant improvement of those published in 2012 for the public release of the Australian ASTER (version 1) geoscience maps [5,6], not just because ~90% of all pixels now provide compositional information (<60% in 2012) but also because these pixels provide more accurate mineral information. Whether this improvement assists in the journey of capturing the value of the Australian ASTER reflectance/emissivity mosaic [34], and ideally the entire ASTER Global Data Archive [116], remains to be seen. However, we also recognize that even though this opportunity can deliver significantly new and unique geoscience information, the level of mineralogical detail is constrained by the ASTER's (multi) spectral resolution and spatial (30–90 m pixel) sampling. The current suite of operational, hyperspectral VNIR–SWIR imaging systems, including (a) China's GF-5; (b) Italy's PRISMA; (c) Japan's HISUI; (d) Germany's EnMap; and the (e) USA's EMIT, should, in theory, improve the specificity of this mineral information. Indeed, NASA has just published a preliminary, composite hematite–goethite–kaolinite mineral map of the world's desert regions [117], including a large part of the Australian continent. From these data, a more precise map of AlOH-bearing minerals can, in theory, be generated, as well as a (much) better estimation of the dry vegetation cover, e.g., using the 2080 nm cellulose absorption rate. At any rate, ASTER's multispectral VNIR–SWIR–TIR global data archive provides a historical baseline of the Earth's land surface composition of the early 2000s, which, following appropriate processing, has the potential to still surprise us with new and valuable geoscience information.

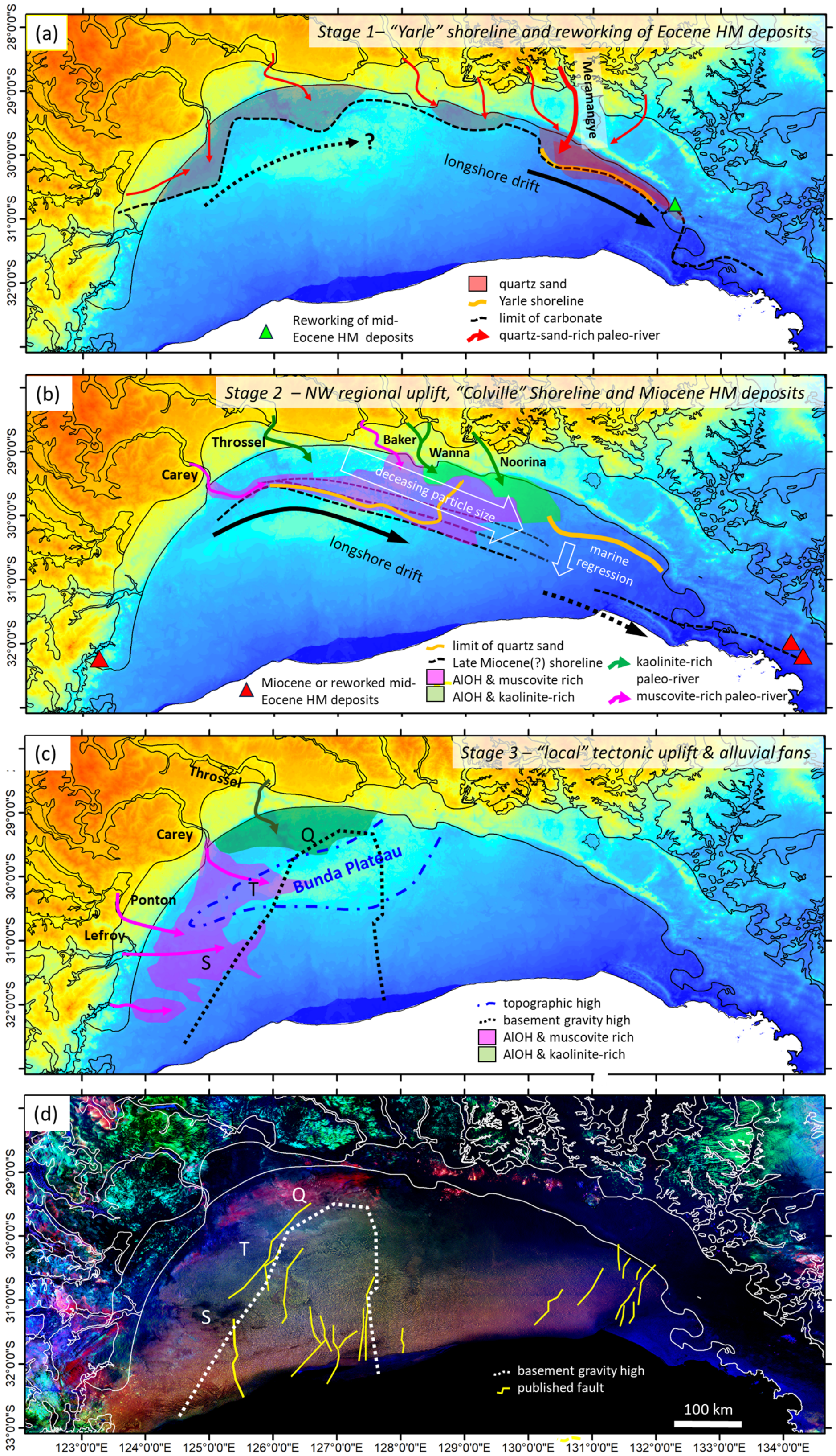

Figure 9. Geomorphic reconstruction of the Miocene Eucla Basin based on the ASTER mineral maps (Figure 8) for chronological geomorphic stages 1 (**a**); 2 (**b**); and 3 (**c**). (**a**–**c**) use a DEM [51] as the base map (warmer colors are higher elevation), while (**d**) uses a ternary gamma radiometric map (R:G:B; K:Th:U) [53]. The boundary of a basement rock gravity and magnetic high feature [118] is shown as a dotted line in Figure (**c**,**d**). Yellow lines in (**d**) are faults with surface expression [112]. Q, S and T are locations referred to in the body text.

5. Conclusions

This study aimed to improve the geoscience information content extractable from the publicly available Australian ASTER reflectance/emissivity mosaic [5,6,34] through a reassessment of selected spectral indices used to generate selected mineral products suitable for mapping (paleo)geomorphic features across the arid parts of Australia, including the silica index (~quartz sand content), AlOH content and composition (e.g., kaolinite and muscovite/illite), and water content. In particular, these ASTER products were tested using an unmixing strategy to suppress/remove the effects of both the green and dry vegetation components to leave, as residual, the target surface mineral information. These results were validated using the NGSA field sample data suite, as well as by visual improvements in the derived imagery at different spatial scales. The major results include:

1. The AlOH content is more accurately gauged using B_7/B_6;
2. The AlOH composition is more accurately gauged using B_7/B_5, though in color imagery, we recommend a R:G:B combination of B_7/B_6: B_7/B_5: B_7/B_6;
3. The water content is more accurately gauged using $(B_5 + B_8)/(B_7 + B_9)$;
4. Despite the ASTER's lack of spectral bands covering diagnostic dry vegetation features, both N-SWIR (Equation (2)) and TIR (Equation (3)) band combinations yield useful approximations, albeit with some residual mineral information remaining and the N-SWIR index showing lesser artefacts (and better pixel resolution);
5. The ASTER vegetation unmixing strategy requires a stepwise, iterative approach to assess whether vegetation is compromising the pixel mineral information. We recommend using both 2D scattergrams of the target mineral and vegetation indices, a selection of appropriate scale factors (gains in Equation (4)), and a visual assessment of the resultant unmixed imagery. Note that the size of the gains used in the unmixing algorithm can have pronounced, potentially erroneous effects on the derived product if not properly gauged;
6. The AlOH content/composition and silica index products were compromised by vegetation, but the water content product was not;
7. At a continental-scale, the vegetation unmixing suppresses/removes the vegetation patterns driven by climate-driven rainfall, while at the regional-level, the vegetation unmixing removes the effect of fire scars;
8. The new methodology resulted in 90% of the pixels being mapped for mineralogy, in contrast with the 60% provided in the 2012 Australian ASTER mineral products;
9. Vegetation unmixing revealed a regional N–S zonation across the ~25° S latitude, especially in the western half of the continent, characterized by abundant AlOH minerals, especially muscovite, in the south versus less-abundant AlOH minerals, which are relatively kaolinite-rich in the north. This zonation is likely driven by the high-pressure belt and its effect on the prevailing wind patterns and associated transport of aeolian sediment;
10. Vegetation unmixing revealed the paleo-drainage network across the aeolian sand-covered Canning Basin to comprise low AlOH content, similar to the current-day Darling River. In more complex, "upland" geological environments, like the Yilgarn Craton, paleo-rivers have a more complicated, discontinuous surface mineralogical pattern driven by a variety of processes, including catchment rock type and groundwater condition;
11. Vegetation unmixing better maps the composition of paleo-rivers (and their source catchments), Miocene shorelines, and alluvial fans across the Eucla Basin, including the Colville Sandstone, which was distinguished by linear patterns in quartz sand and AlOH minerals that present a new opportunity for heavy mineral sand exploration;
12. We interpreted the updated ASTER maps of the Eucla Basin to show three stages of basin sedimentation, including: (i) stage 1—high-energy shoreline, Yarle Sandstone development related to tectonic uplift in the NE and relatively higher sea level and removal of the AlOH mineral component; (ii) stage 2—lower-energy shoreline, Colville Sandstone development related to westward shift in tectonic uplift and lowering

sea level and the deposition of AlOH minerals from different source regions; and (iii) Stage 3—cessation of the shoreline system caused by a regional westward shift in tectonic uplift coupled with a localized Eucla Basin basement block uplift and lowering sea level resulting in the development of alluvial fans with different AlOH mineral compositions depending on paleo-river catchment rocks;

13. The non-vegetation unmixed water content product revealed a 100 km wide, 600 km long "dry" zone located in the eastern margin of the Yilgarn Craton, apparently associated with a deep tectonic structure (from published seismic data and drilling) and an apparent lack of Archaean gold deposits;
14. A 1000 km wide circular pattern over the Lake Eyre region, characterized by a broad rim of abundant "muscovite" (and other mineral products), is spatially coincident with opal fields. An explanation for this association is to be followed up in future work.

Author Contributions: T.C.: conception, data curation, methodology, analysis, writing; L.C.: data curation. All authors have read and agreed to the published version of the manuscript.

Funding: This research received no external funding.

Data Availability Statement: The ASTER efrfellectance/emissivity data mosaic of Australia is available from Geocience Australia [34]: https://dev.ecat.ga.gov.au/geonetwork/srv/api/records/1a311ac9-66a8-4557-957d-e1c035610711 (accessed on 31 May 2023).

Acknowledgments: I would like to thank my ASTER colleagues from around the world who helped achieve the vision of creating a complete suite of ASTER geoscience maps of Australia (see [6] for details). This paper commemorates the short life of William (Liam) Johannes Cudahy (5 April 1996 to 30 May 2021). Liam was beginning his career as an environmental scientist when the COVID-19 pandemic and its associated lockdowns caused him to postpone his university honors research project at the University of Western Australia on "Soil properties of variably-performing rehabilitated lands associated with the Greenbushes mine, Western Australia". Liam's honors thesis was to be based on processed multi-temporal satellite imagery using the unmixing techniques presented in this paper.

Conflicts of Interest: TC is a Director of C3DMM Pty Ltd. and LC was a former employee of C3DMM Pty Ltd. The research was conducted in the absence of any commercial or financial relationships that could be construed as a potential conflict of interest.

References

1. Yamaguchi, Y.; Kahle, A.B.; Tsu, H.; Kawakami, T.; Pniel, M. Overview of Advanced Spaceborne Thermal Emission and Reflection Radiometer (ASTER). *IEEE Trans. Geosci. Remote* **1998**, *36*, 1062–1071. [CrossRef]
2. Clark, R.N. Spectroscopy of rocks and minerals, and principles of spectroscopy. In *Manual of Remote Sensing*; Rencz, A., Ed.; John Wiley and Sons Inc.: New York, NY, USA, 1999; Chapter 1.
3. Meyer, J.M.; Kokaly, R.F.; Holley, E. Hyperspectral remote sensing of white mica: A review of imaging and point-based spectrometer studies for mineral resources, with spectrometer design considerations. *Remote Sens. Environ.* **2022**, *275*, 113000. [CrossRef]

4. Rouxhet, P.G.; Samudacheata, N.; Jacobs, H.; Anton, O. Attribution of the OH stretching bands of kaolinite. *Clay Miner.* **1977**, *12*, 171–179. [CrossRef]
5. Cudahy, T. *Satellite ASTER Geoscience Product Notes for Australia*; EP125895; CSIRO: Canberra, Australia, 2012. [CrossRef]
6. Cudahy, T.J.; Caccetta, M.; Thomas, M.; Hewson, R.; Abrams, M.; Kato, M.; Kashimura, O.; Ninomiya, Y.; Yamaguchi, Y.; Collings, S.; et al. Satellite-derived mineral mapping and monitoring of weathering, deposition and erosion. *Sci. Rep.* **2016**, *6*, 23702. [CrossRef] [PubMed]
7. Cudahy, T. Mineral Mapping for Exploration: An Australian Journey of Evolving Spectral Sensing Technologies and Industry Collaboration. *Geosciences* **2016**, *6*, 52. [CrossRef]
8. Hewson, R.; Robson, D.; Mauger, A.; Cudahy, T.; Thomas, M.; Jones, M. Using the Geoscience Australia-CSIRO ASTER maps and airborne geophysics to explore Australian geoscience. *J. Spat. Sci.* **2015**, *60*, 207–231. [CrossRef]
9. Hewson, R.; Robson, D.; Carlton, A.; Gilmore, P. Geological application of ASTER remote sensing within sparsely outcropping terrain, Central New South Wales, Australia. *Cogent Geosci.* **2017**, *3*, 1319259. [CrossRef]
10. Lampinen, H.M.; Laukamp, C.; Occhipinti, S.A.; Metelka, V.; Spinks, S.C. Delineating alteration footprints from field and ASTER SWIR spectra, geochemistry, and gamma-ray spectrometry above regolith-covered base metal deposits—An example from Abra, Western Australia. *Econ. Geol.* **2017**, *112*, 1977–2003. [CrossRef]
11. Lau, I.C.; Cudahy, T.J.; Caccetta, M.C.; Kobayashi, C.; Kashimura, O.; Kato, M. Proximal, remote sensing and spectroscopy of soil Mapping surface soil mineralogy using hyperspectral and ASTER imagery: An example from Mullewa, Western Australia. In *Digital Soil Assessments and Beyond*; CRC Press: Boca Raton, FL, USA, 2012; ISBN 9780429097461.
12. Laukamp, C.; Cudahy, T.; Caccetta, M.; Thomas, M.; Close, D.; Lennartz, R. Successful mineral exploration using multispectral remote sensing data—ASTER geoscience Map of Australia. In Proceedings of the 12th SGA Biennial Meeting, Uppsala, Sweden, 12–15 August 2013. 4p.
13. Laukamp, C.; Salama, W.; González-Álvarez, I. Proximal and remote spectroscopic characterisation of regolith in the Albany–Fraser Orogen (Western Australia). *Ore Geol. Rev.* **2016**, *73*, 540–554, ISSN 0169-1368. [CrossRef]
14. Mernagh, T.P.; Bastrakov, E.N.; Clarke, J.D.A.; de Caritat, P.; English, P.M.; Howard, F.J.F.; Jaireth, S.; Magee, J.W.; McPherson, A.A.; Roach, I.C.; et al. *A Review of Australian Salt Lakes and Assessment of Their Potential for Strategic Resources*; Record 2013/039; Geoscience Australia: Canberra, Australia, 2013. Available online: https://pid.geoscience.gov.au/dataset/ga/76454 (accessed on 10 May 2023).
15. Rutherford, J.; Cendón, D.I.; Soerensen, C.; Batty, S.; Huntley, B.; Bourke, L.; Pinder, A.; Quinlan, K.; English, V.; Coote, M. *Hydrological Conceptualisation of the Walyarta Mound Springs*; Department of Biodiversity, Conservation and Attractions, Wetlands Conservation Program: Perth, Australia, 2018. Available online: https://library.dbca.wa.gov.au/static/FullTextFiles/072271.pdf (accessed on 15 February 2023).
16. Rouse, J.W.; Haas, R.H.; Scheel, J.A.; Deering, D.W. Monitoring Vegetation Systems in the Great Plains with ERTS. In Proceedings of the 3rd Earth Resource Technology Satellite (ERTS) Symposium, Washington, DC, USA, 10–14 December 1974; Volume 1, pp. 48–62. Available online: https://ntrs.nasa.gov/citations/19740022614 (accessed on 4 April 2024).
17. Elvidge, C.D. Thermal Infrared Reflectance of Dry Plant Materials: 2.5–20.0um. *Remote Sens. Environ.* **1998**, *26*, 265–285. [CrossRef]
18. Serbin, G.; Hunt, E.R., Jr.; Daughtry, C.S.T.; McCarty, G.W.; Doraiswamy, P.C. An improved ASTER index for remote sensing of crop residue. *Remote Sens.* **2009**, *1*, 971–991. [CrossRef]
19. Gill, T.K.; Phinn, S. Estimates of bare ground and vegetation cover from Advanced Spaceborne Thermal Emission and Reflection Radiometer (ASTER) short-wave-infrared reflectance imagery. *J. Appl. Remote Sens.* **2008**, *2*, 023511. [CrossRef]
20. Lehmann, E.A.; Wallace, J.F.; Caccetta, P.; Zdunic, K. Forest cover trends from time series Landsat data for the Australian continent. *Int. J. Appl. Earth Obs. Geoinf.* **2013**, *21*, 453–462. [CrossRef]
21. Cudahy, T.J.; Jones, M.; Lisitsin, V.A.; Caccetta, M.; Collings, S.; Bateman, R. *3D Mineral Mapping of Queensland—Version 2 ASTER and Related Geoscience Products*; EP17697; CSIRO: Kensington, Australia, 2017. [CrossRef]
22. Caccetta, M.; Cudahy, T.; Ong, C.; Lau, I. An investigation into the use of the thermal wavelengths of the ASTER satellite borne sensor for dry vegetation identification. In Proceedings of the IGARSS 2016—2016 IEEE International Geoscience and Remote Sensing Symposium, Beijing, China, 10–15 July 2016; pp. 1943–1946. [CrossRef]
23. Salisbury, J.W. Preliminary measurements of leaf spectral reflectance in the 8–14 μm region. *Int. J. Remote Sens.* **1986**, *7*, 1879–1886. [CrossRef]
24. Craig, M.A. Unsupervised unmixing of remotely sensed images. In Proceedings of the 5th Australasian Remote Sensing Conference, Perth, Australia, 8–12 October 1990; pp. 324–330.
25. Bierwirth, P.N. Mineral mapping and vegetation removal via data-calibrated pixel unmixing, using multispectral images. *Int. J. Remote Sens.* **1990**, *11*, 1999–2017. [CrossRef]
26. Boardman, J. Automating Spectral Unmixing of AVIRIS Data Using Convex Geometry Concepts. In Proceedings of the Summaries of the 4th Annual JPL Airborne Geoscience Workshop, Washington, DC, USA, 25–29 October 1993; pp. 11–14.
27. Craig, M.D. Minimum volume transformations for remotely sensed data. *IEEE Trans. Geosci. Remote Sens.* **1994**, *32*, 542–552. [CrossRef]
28. Staenz, K.; Nadeau, C.; Secker, J.; Budkewitsch, P. Spectral unmixing applied to vegetated environments in the Canadian Artic for mineral mapping. *Int. Arch. Photogramm. Remote Sens.* **2000**, *33*, 1464–1471.

29. Asner, G.P.; Heidebrecht, K.B. Spectral unmixing of vegetation, soil and dry carbon in arid regions: Comparing multispectral and hyperspectral observations. *Int. J. Remote Sens.* **2002**, *23*, 3939–3958. [CrossRef]
30. Rodger, R.; Cudahy, T. Vegetation corrected continuum depths at 2.20 µm: An approach for hyperspectral sensors. *Remote Sens. Environ.* **2009**, *113*, 2243–2257. [CrossRef]
31. Grebby, S.; Cunningham, D.; Tansey, K.; Naden, J. The Impact of Vegetation on Lithological Mapping Using Airborne Multispectral Data: A Case Study for the North Troodos Region, Cyprus. *Remote Sens.* **2014**, *6*, 10860–10887. [CrossRef]
32. Haest, M.; Cudahy, T.; Rodger, A.; Laukamp, C.; Martens, E.; Caccetta, M. Unmixing the effects of vegetation in airborne hyperspectral mineral maps over the Rocklea Dome iron-rich palaeochannel system (Western Australia). *Remote Sens. Environ.* **2013**, *129*, 17–31. [CrossRef]
33. De Souza Kovacs, N.; Cudahy, T.J. *Regolith–Landform Mapping of the West Kimberley Craton: Application of Geophysics and Spectral Remote Sensing*; Report 231; Geological Survey of Western Australia: Perth, Australia, 2022; 87p.
34. Australian ASTER Reflectance/Emissivity Mosaic. Geoscience Australia, Canberra. Available online: https://dev.ecat.ga.gov.au/geonetwork/srv/api/records/1a311ac9-66a8-4557-957d-e1c035610711 (accessed on 31 May 2023).
35. Caccetta, M.; Collings, S.; Cudahy, T. A calibration methodology for continental-scale mapping using ASTER imagery. *Remote Sens. Environ.* **2013**, *139*, 306–317. [CrossRef]
36. De Caritat, P.; Cooper, M. *National Geochemical Survey of Australia: The Geochemical Atlas of Australia*; Record 2011/20; Geoscience Australia: Canberra, Australia, 2011; 557p.
37. De Caritat, P. The National Geochemical Survey of Australia: Review and impact. *Geochem. Explor. Environ. Anal.* **2022**, *22*, geochem2022-032. [CrossRef]
38. Lau, I.C.; Laukamp, C.; Bateman, R.; Beattite, E.; de Caritat, P.; Ong, C.; Thomas, M.; Caccetta, M.; Wang, R.; Cudahy, T. *Spectral Reflectance Measurement Procedures for Soil and Powder Samples*; Report number: E18382; The Commonwealth Scientific and Industrial Research Organisation (CSIRO): Canberra, Australia, 2018; 39p.
39. Boreham, C.J.; Edwards, D.S.; Czado, K.; Rollet, N.; Wang, L.; van der Weilen, S.; Champion, D.; Blewett, R.; Feitz, A.; Henson, P.A. Hydrogen in Australian natural gas: Occurrences, sources and resources. *APPEA J.* **2021**, *61*, 163–191. [CrossRef]
40. Wyrwoll, K.-H. Time in the geomorphology of Western Australia. *Prog. Phys. Geogr. Earth Environ.* **1988**, *12*, 237–263. [CrossRef]
41. Tapley, I.J. The reconstruction of palaeodrainage and regional geologic structures in Australia's Canning and Officer Basins using NOAA–AVHRR satellite imagery. *Earth Sci. Rev.* **1988**, *25*, 409–425. [CrossRef]
42. Kern, A.M.; Commander, D.P. Cainozoic stratigraphy in the Roe Palaeodrainage of the Kalgoorlie region, Western Australia. *Geol. Surv. West. Aust. Prof. Pap.* **1993**, *34*, 85–95. Available online: https://geodocs.dmirs.wa.gov.au/Web/documentlist/3/Combined/N91CP/H (accessed on 1 July 2023).
43. Morgan, K.H. Development, sedimentation and economic potential of palaeoriver systems of the Yilgarn Craton of Western Australia. *Sediment. Geol.* **1993**, *85*, 637–656, ISSN 0037-0738. [CrossRef]
44. Hou, B.; Keeling, J.; Li, Z. Paleovalley-related uranium deposits in Australia and China: A review of geological and exploration models and methods. *Ore Geol. Rev.* **2017**, *88*, 201–234, ISSN 0169-1368. [CrossRef]
45. De Broekert, P.; Sandiford, M. Buried Inset-Valleys in the Eastern Yilgarn Craton, Western Australia: Geomorphology, Age, and Allogenic Control. *J. Geol.* **2005**, *113*, 471–493. [CrossRef]
46. George, R.; Clarke, J.; English, P. Modern and palaeogeographic trends in the salinisation of the Western Australian Wheatbelt. *ASEG Ext. Abstr.* **2006**, *1*, 1–22. [CrossRef]
47. Bell, J.G.; Kilgour, P.L.; English, P.M.; Woodgate, M.F.; Lewis, S.J. *WASANT Palaeovalley Map—Distribution of Palaeovalleys in Arid and Semi-Arid WA-SA-NT*; Geoscience Australia: Canberra, Australia, 2012. Available online: https://ecat.ga.gov.au/geonetwork/srv/eng/catalog.search#/metadata/73980 (accessed on 14 February 2023).
48. Pain, C.F.; Pillans, B.J.; Roach, I.A.; Worrall, L.; Wilford, J.R. Old, flat and red—Australia's distinctive landscape. In *Shaping a Nation: A Geology of Australia*; Blewett, R.S., Ed.; ANU Press: Canberra, Australian, 2012; Chapter 5; pp. 227–276.
49. Brocard, G.; Ding, X.; Salles, T.; Zahirovic, S.; Rey, P.; Möller, D. Transcontinental Cainozoic paleovalleys of Western Australia. *ASEG Ext. Abstr.* **2018**, *1*, 1–6. [CrossRef]
50. Hou, B.; Keeling, J.; Reid, A.; Petts, A.; Stoian, L. *Eucla Basin and Peripheral Paleovalleys*; Report Book 2022/00011; Department for Energy and Mining, South Australia: Adelaide, Australia, 2022; 131p.
51. Hutchinson, M.F.; Stein, J.L.; Stein, J.A.; Anderson, H.; Tickle, P.K. *GEODATA 9 Second DEM and D8: Digital Elevation Model Version 3 and Flow Direction Grid 2008*; Record DEM-9S.v3; Geoscience Australia: Canberra, Australia, 2008. Available online: http://pid.geoscience.gov.au/dataset/ga/66006 (accessed on 10 May 2023).
52. Jakica, S.; Brisbout, L.; de Souza Kovacs, N. *Applying Geophysics for 3D Paleochannel Imaging in the Gascoyne Province, Western Australia*; Record 2021/7; Geological Survey of Western Australia: Perth, Australia, 2021; 27p.
53. Radiometric Grid of Australia (Radmap) v4 2019—Ternary Image (K, Th, U). Geoscience Australia. Available online: https://ecat.ga.gov.au/geonetwork/srv/eng/catalog.search#/metadata/134857 (accessed on 13 March 2019).
54. Hou, B.; Keeling, J.; van Gosen, B.S. Geological and exploration models of beach placer deposits, integrated from case-studies of Southern Australia. *Ore Geol. Rev.* **2017**, *80*, 437–459. [CrossRef]
55. Ninomiya, Y. Quantitative estimation of SiO_2 content in igneous rocks using thermal infrared spectra with a neural network approach. *IEEE Trans. Geosci. Remote Sens.* **1995**, *33*, 684–691. [CrossRef]

56. Hook, S.J.; Dmochowski, J.E.; Howard, K.A.; Rowan, L.C.; Karlstrom, K.E.; Stock, J.M. Mapping variations in weight percent silica measured from multispectral thermal infrared imagery—Examples from the Hiller Mountains, Nevada, USA and Tres Virgenes-La Reforma, Baja California Sur, Mexico. *Remote Sens. Environ.* **2005**, *95*, 273–289, ISSN 0034-4257. [CrossRef]
57. Post, J.L.; Noble, P.N. The Near-Infrared Combination Band Frequencies of Dioctahedral Smectites, Micas, and Illites. *Clays Clay Miner.* **1993**, *41*, 639–644. [CrossRef]
58. Crowley, J.K.; Brickey, D.W.; Rowan, L.C. Airborne imaging spectrometer data of the Ruby Mountains, Montana: Mineral discrimination using relative absorption band-depth images. *Remote Sens. Environ.* **1989**, *29*, 121–134. [CrossRef]
59. Green, A.A.; Craig, M.D. Analysis of aircraft spectrometer data with logarithmic residuals. In *Proceedings of the Airborne Imaging Spectrometer Workshop, Pasadena, CA, USA, 8–10 April 1985*; Vane, G., Goetz, A.F.H., Eds.; JPL Publication 85-41; JPL: Pasadena, CA, USA, 1985; pp. 111–119.
60. Feng, J.; Rivard, B.; Sánchez-Azofeifa, A. The topographic normalization of hyperspectral data: Implications for the selection of spectral end members and lithologic mapping. *Remote Sens. Environ.* **2003**, *85*, 221–231, ISSN 0034-4257. [CrossRef]
61. Iwasaki, A.; Tonooka, H. Validation of a crosstalk correction algorithm for ASTER/SWIR. *IEEE Trans. Geosci. Remote Sens.* **2005**, *43*, 2747–2751. [CrossRef]
62. Murphy, R.J.; Wadge, G. The effects of vegetation on the ability to map soils using imaging spectrometer data. *Int. J. Remote Sens.* **1994**, *15*, 63–86. [CrossRef]
63. Luz, B.; Crowley, J. Spectral reflectance and emissivity features of broad leaf plants: Prospects for remote sensing in the thermal infrared (8.0–14.0 μm). *Remote Sens. Environ.* **2007**, *109*, 393–405. [CrossRef]
64. Milliken, R.E.; Mustard, J.F. Quantifying absolute water content of minerals using near-infrared reflectance spectroscopy. *J. Geophys. Res.* **2005**, *110*, E12001. [CrossRef]
65. Nesbitt, H.W.; Young, G.M. Early Proterozoic climates and plate motions inferred from major element chemistry of lutites. *Nature* **1982**, *299*, 715–717. [CrossRef]
66. Lechler, P.J.; Desilets, M.O. A review of the use of loss on ignition as a measurement of total volatiles in whole-rock analysis. *Chem. Geol.* **1987**, *63*, 341–344, ISSN 0009-2541. [CrossRef]
67. Cooper, D.C.; Mustard, J.F. Effects of very Fine Particle Size on reflectance spectra of smectite and palagonitic soil. *Icarus* **1999**, *142*, 557–570. [CrossRef]
68. Low, P.F.; White, J.L. Hydrogen bonding and polywater in clay-water systems. *Clays Clay Miner.* **1970**, *18*, 63–66. [CrossRef]
69. Moenke, H.H.W. Vibrational Spectra and the Crystal-chemical Classification of Minerals. In *The Infrared Spectra of Minerals*; Farmer, V.C., Ed.; Mineralogical Society of Great Britain and Ireland: Londan, UK, 1974; pp. 111–118. [CrossRef]
70. Gray, D.J. *Spectral Reflectance Studies of the Impact of Water on Mineral Spectra*; CSIRO/AMIRA Project P435, Report 444R; Australian Mineral Industries Research Association, Ltd.: Parkville, Australia, 1997; 82p.
71. Chen, X.Y.; McKenzie, N.J.; Roach, I.C. Distribution in Australia: Calcrete landscapes. In *Calcrete: Characteristics, Distribution and Use in Mineral Exploration*; Chen, X.Y., Lintern, M.J., Roach, I.C., Eds.; Cooperative Research Centre for Landscape Environments and Mineral Exploration: Bentley, Australia, 2002; pp. 110–138, ISBN 0-9581145-0-1. Available online: http://crcleme.org.au/Pubs/Monographs/Calcrete%20Book%20-%20FINAL.pdf (accessed on 22 February 2023).
72. Fraser, S.J.; Green, A.A. A software defoliant for geological analysis of band ratios. *Int. J. Remote Sens.* **1987**, *8*, 525–532. [CrossRef]
73. Sánchez, F.G.; Luc, R.; Van Loon, L.R.; Gimmi, T.; Jakob, A.; Glaus, M.A.; Diamond, L.W. Self-diffusion of water and its dependence on temperature and ionic strength in highly compacted montmorillonite, illite and kaolinite. *Appl. Geochem.* **2008**, *23*, 3840–3851. [CrossRef]
74. Duda, K.; Daucsavage, J. *Advanced Spaceborne Thermal Emission and Reflection Radiometer (ASTER) Level 1 Precision Terrain Corrected Registered At-Sensor Radiance Product (AST_L1T)—AST_L1T Product User's Guide*; Version 1.1; USGS EROS Data Center, Sioux Falls South Dakota: Sioux Falls, SD, USA, 2020. Available online: https://lpdaac.usgs.gov/documents/647/AST__L1T_User_Guide_V3.pdf (accessed on 11 February 2024).
75. Anand, R.R.; Paine, M. Regolith geology of the Yilgarn Craton, Western Australia: Implications for exploration. *Aust. J. Earth Sci.* **2002**, *49*, 3–162. [CrossRef]
76. Groeneveld, J.; Henderiks, J.; Renema, W.; McHugh, C.M.; De Vleeschouwer, D.; Christensen, B.A.; Fulthorpe, C.S.; Reuning, L.; Gallagher, S.J.; Bogus, K.; et al. Australian shelf sediments reveal shifts in Miocene Southern Hemisphere westerlies. *Sci. Adv.* **2017**, *3*, e1602567. [CrossRef]
77. Kennett, B. *AusMoho, Australian Passive Seismic Server (AusPass) and the Australian National University Data Commons*; ANU Press: Canberra, Australia, 2019. [CrossRef]
78. Sandiford, M. The tilting continent: A new constraint on the dynamic topographic field from Australia. *Earth Planet. Sci. Lett.* **2007**, *261*, 152–163, ISSN 0012-821X. [CrossRef]
79. Butt, C.R.M.; Horwitz, R.C.H.; Mann, A.W. *Uranium Occurrences in Calcrete and Associated Sediments in Western Australia*; Report FP16; CSIRO Division of Mineralogy: Perth, Australia, 1977.
80. Gray, D.J. Hydrogeochemistry in the Yilgarn Craton. *Geochem. Explor. Environ. Anal.* **2001**, *1*, 253–264. [CrossRef]
81. Hocking, R.M. *In Geology and Mineral Resources of Western Australia*; Memoir 3; Geological Survey of Western Australia: Perth, Australia, 1990; pp. 548–561.

82. Hocking, R.M.; Mory, A.J.; Williams, I.R. *An Atlas of Neoproterozoic and Phanerozoic Basins of Western Australia*; Petroleum Exploration Society of Australia (PESA): Beaumaris, Australia, 1994; 34p. Available online: https://pesa.com.au/the_sedimentary_basins_of_wa_p21-43-pdf (accessed on 30 May 2023).
83. English, P.; Lewis, S.; Bell, J.; Wischusen, J.; Woodgate, M.; Bastrakov, E.; Macphail, M.; Kilgour, P. *Water for Australia's Arid Zone—Identifying and Assessing Australia's Palaeovalley Groundwater Resources: Summary Report*; Waterlines report; National Water Commission: Canberra, Australia, 2012; 129p, ISBN 978-1-922136-01-5.
84. Buckingham, W.F.; Sommer, S.E. Mineralogical characterization of rock surfaces formed by hydrothermal alteration and weathering—Application to remote sensing. *Econ. Geol.* **1983**, *78*, 664–674. [CrossRef]
85. Clark, R.N. Spectral properties of mixtures of montmorillonite and dark carbon grains: Implications for remote sensing minerals containing chemically and physically absorbed water. *J. Geophys. Res.* **1983**, *88*, 10635–10644. [CrossRef]
86. Geoview, W.A. The Geological Survey of Western Australia's Interactive Geological Map. Available online: https://www.dmp.wa.gov.au/GeoView-WA-Interactive-1467.aspx (accessed on 16 February 2023).
87. Haines, P.W.; Hocking, R.M.; Grey, K.; Stevens, M.K. Vines 1 revisited: Are older Neoproterozoic glacial deposits preserved in Western Australia? *Aust. J. Earth Sci.* **2008**, *55*, 397–406. [CrossRef]
88. Beard, J.S. Palaeogeography and drainage evolution in the Gibson and Great Victoria Deserts, Western Australia. *J. R. Soc. West. Aust.* **2002**, *85*, 17–29. Available online: https://www.biodiversitylibrary.org/partpdf/298673 (accessed on 10 September 2023).
89. Hou, B.; Frakes, L.; Sandiford, M.; Worrall, L.; Keeling, J.; Alley, N.F. Cenozoic Eucla Basin and associated palaeovalleys, southern Australia—climatic and tectonic influences on landscape volution, sedimentation and heavy mineral accumulation. *Sediment. Geol.* **2008**, *203*, 112–130. [CrossRef]
90. Ward, S.H. Gamma-ray spectrometry in geological mapping and uranium exploration. *Econ. Geol.* **1981**, *75*, 840–849.
91. Potter, R.M.; Rossman, G.R. Desert Varnish: The Importance of Clay Minerals. *Science* **1977**, *196*, 1446–1448. [CrossRef]
92. Gray, D.J.; Bardwell, N. *Hydrogeochemistry of Western Australia: Data Release: Accompanying Notes*; EP156404; CSIRO: Canberra, Australia, 2016; 33p. [CrossRef]
93. Gray, D.J.; Reid, N.; Noble, R.; Thorne, R.; Giblin, A. *Hydrogeochemical Mapping of the Australian Continent*; EP195905; CSIRO: Canberra, Australia, 2019; 110p. [CrossRef]
94. Groves, D.I.; Phillips, G.N.; Ho, S.E.; Houston, S.M.; Standing, C.A. Craton-scale distribution of Archean greenstone gold deposits; predictive capacity of the metamorphic model. *Econ. Geol.* **1987**, *82*, 2045–2058. [CrossRef]
95. Korsch, R.J.; Blewett, R.S.; Smithies, R.H.; Quentin de Gromard, R.; Howard, H.M.; Pawley, M.J.; Carr, L.K.; Hocking, R.M.; Neumann, N.L.; Kennett, B.L.N.; et al. Geological setting and interpretation of the southwest half of deep seismic reflection line 11GA-YO1: Yamarna Terrane of the Yilgarn Craton and the western Officer Basin. In *Yilgarn Craton–Officer Basin–Musgrave Province Seismic and MT Workshop Edition*; Record, 2013/28; Neumann, N.L., Ed.; Geoscience Australia: Canberra, Australia, 2013; Chapter 3.
96. Grey, K.; Hocking, R.M.; Stevens, M.K.; Bagas, L.; Carlsen, G.M.; Irimies, F.; Pirajno, F.; Haines, P.W.; Apak, S.N. *Lithostratigraphic Nomenclature of the Officer Basin and Correlative Parts of the Paterson Orogen, Western Australia*; Report 93; Western Australia Geological Survey: Perth, Australia, 2005; 89p.
97. Gartmair, G.; Barham, M.; Kirkland, C.L. Detrital Zircon Perspectives on Heavy Mineral Sand Systems, Eucla Basin, Australia. *Econ. Geol.* **2022**, *117*, 383–399. [CrossRef]
98. Auscope National Virtual Core Library (NVCL). Available online: https://www.auscope.org.au/nvcl (accessed on 13 February 2024).
99. Goleby, B.R.; Blewett, R.S.; Korsch, R.J.; Champion, D.C.; Cassidy, K.F.; Jones, L.E.A.; Groenewald, P.B.; Henson, P. Deep seismic reflection profiling in the Archaean northeastern Yilgarn Craton, Western Australia: Implications for crustal architecture and mineral potential. *Tectonophysics* **2009**, *388*, 119–133. [CrossRef]
100. Lowry, D.C. *Geology of the Western Australian Part of the Eucla Basin*; Bulletin 122; Geological Survey of Western Australia: Perth, Australia, 1970; pp. 1–200.
101. Jones, B.G. Cretaceous and Tertiary sedimentation on the western margin of the Eucla Basin. *Aust. J. Earth Sci.* **1990**, *37*, 317–329. [CrossRef]
102. James, N.P.; Bone, Y. Origin of a cool-water, Oligo-Miocene deep shelf limestone, Eucla Platform, southern Australia. *Sedimentology* **1991**, *38*, 323–341.
103. Feary, D.A.; James, N.P. Cenozoic biogenic mounds and buried Miocene(?) barrier reef on a predominantly cool-water carbonate continental margin—Eucla basin, western Great Australian Bight. *Geology* **1995**, *23*, 427–430. [CrossRef]
104. Martin, D.M.B.; Hocking, R.M.; Riganti, A.; Tyler, I.M. *Geological Map of Western Australia, 14th Edition—Explanatory Notes*; Record 2015/14; Geological Survey of Western Australia: Perth, Australia, 2016; 16p, ISBN 978-1-74168-669-2.
105. O'Connell, L.G.; James, N.P.; Bone, Y. The Miocene Nullarbor Limestone, southern Australia; deposition on a vast subtropical epeiric platform. *Sediment. Geol.* **2012**, *253–254*, 1–16, ISSN 0037-0738. [CrossRef]
106. SARIG South Australian Resources Information Gate. Available online: https://map.sarig.sa.gov.au/ (accessed on 17 February 2024).
107. Ninomiya, Y.; Fu, B. Regional Lithological Mapping Using ASTER-TIR Data: Case Study for the Tibetan Plateau and the Surrounding Area. *Geosciences* **2016**, *6*, 39. [CrossRef]

108. Grechi, G.; Fiorucci, M.; Marmoni, G.M.; Martino, S. 3D Thermal Monitoring of Jointed Rock Masses through Infrared Thermography and Photogrammetry. *Remote Sens.* **2021**, *13*, 957. [CrossRef]
109. Stephenson, R.; Lambeck, K. Erosion-isostatic rebound models for uplift: An application to south-eastern Australia. *Geophys. J. R. Astr. Soc.* **1985**, *82*, 31–55. [CrossRef]
110. Spaggiari, C.V.; Smithies, R.H. *Eucla Basement Stratigraphic Drilling Results Release Workshop: Extended Abstracts*; Record 2015/10; Geological Survey of Western Australia: Perth, Australia, 2015.
111. O'Leary, M.; Mounsher, L.; Barham, M.; Timms, N. Cenozoic records of dynamic topography, neotectonics and eustasy from the Eucla Basin. In *Eucla Basement Stratigraphic Drilling Results Release Workshop: Extended Abstracts*; Spaggiari, C.V., Smithies, R.H., Eds.; Record 2015/10; Geological Survey of Western Australia: Perth, Australia, 2015; pp. 4–6.
112. Mounsher, L.C. *Evolution and Deformation of the Onshore Eucla Basin during the Cenozoic*; Record 2016/10; Geological Survey of Western Australia: Perth, Australia, 2016; 70p, ISBN 978-1-74168-695-1.
113. Gingele, F.X.; De Deckker, P.; Hillenbrand, C.D. Clay mineral distribution in surface sediments between Indonesia and NW Australia—Source of transport by ocean currents. *Mar. Geol.* **2001**, *179*, 135–146. [CrossRef]
114. Griffin, J.J.; Windom, H.; Goldberg, E.D. The distribution of clay minerals in the world oceans. *Deep-Sea Res.* **1968**, *15*, 433–459. [CrossRef]
115. Reid, A.; Keeling, J.; Boyd, D.; Belousova, E.; Hou, B. Source of zircon in world-class heavy mineral placer deposits of the Cenozoic Eucla Basin, southern Australia from LA-ICPMS U–Pb geochronology. *Sediment. Geol.* **2012**, *286–287*, 1–19. [CrossRef]
116. Japan Space Systems. Satellite ASTER Data Search. Available online: https://gbank.gsj.jp/madas/map/index.html (accessed on 31 May 2023).
117. NASA's EMIT Mineral Maps of the Earth's Desert Regions. Available online: https://www.nasa.gov/missions/emit/nasa-sensor-produces-first-global-maps-of-surface-minerals-in-arid-regions (accessed on 21 April 2024).
118. Geoscience Australia. Geophysics Maps of Australia. Available online: https://www.ga.gov.au/scientific-topics/disciplines/geophysics (accessed on 8 March 2024).